Computer Methods in Applied Mechanics and Engineering 448 (2026) 118500

Contents lists available at ScienceDirect

Comput. Methods Appl. Mech. Engrg.

journal homepage: www.elsevier.com/locate/cma

Robust sequential algorithm for plasticity–micromorphic damage coupling in polycrystalline ductile fracture analysis

Tianwen Tan [a,b], Ikumu Watanabe [a,b,*]

[a] Graduate School of Pure and Applied Sciences, University of Tsukuba, 1-1-1 Tennodai, Tsukuba, 305-8573, Japan
[b] Center for Basic Research on Materials, National Institute for Materials Science, 1-2-1 Sengen, Tsukuba, 305-0047, Japan

ARTICLE INFO

Keywords:
Ductile fracture
Rate–independent single crystal plasticity
Robustness
Micromorphic damage mechanism
Finite strain

ABSTRACT

Numerical simulations of ductile fracture analysis frequently encounter significant convergence challenges. While existing efforts have largely focused on global/local numerical optimization or extended (discontinuous) methods, this study introduces a novel stress-update algorithm operating at the material point level. This algorithm is designed to mitigate the computational difficulties inherent in ductile fracture problems, especially in single crystal plasticity simulations that employ rate–independent constitutive formulations. For implicit models based on continuum damage mechanics, material softening mechanisms like damage complicate the solution of global equations. This study demonstrates that the plasticity mechanism can be locally separated from the damage mechanism while maintaining mathematical equivalence with a conventional algorithm. This sequential scheme provides a robust and convenient approach for describing the coupling between multiple plasticity and damage internal state variables. Furthermore, a micromorphic damage enhancement, serving as a gradient extension, is utilized to mitigate spurious mesh-dependence and to account for the characteristic length scale in polycrystalline systems. The advantages and limitations of the proposed algorithm, from its constitutive formulations to its comparative applications, are thoroughly discussed.

1. Introduction

1.1. Background and aims

Quantitatively characterizing crack initiation and propagation remains a formidable challenge in solid mechanics. Computational approaches are powerful tools for systematically understanding the structural failure process, which encompasses phenomena such as crack initiation induced by microscopic damage accumulation, crack propagation through damage zone growth, crack branching influenced by localized damage behavior, and final crack coalescence. Material fracture responses are categorized as brittle, quasi-brittle, and ductile, each distinguished by specific damage initiation and evolution mechanisms. The numerical performance of these simulations is significantly affected by material instability, which increases considerably from brittle to ductile cases.

For Finite Element Method (FEM)-based approaches, brittle fracture is characterized by a sudden local stiffness drop upon reaching a critical state. This phenomenon adversely affects the global assembled stiffness matrix, leading to ill-conditioning that complicates the solution of global equations [1,2]. To address these numerical challenges, several studies have proposed discontinuous approaches

---

* Corresponding author.
E-mail address: WATANABE.Ikumu@nims.go.jp (I. Watanabe).

https://doi.org/10.1016/j.cma.2025.118500
Received 30 May 2025; Received in revised form 17 August 2025; Accepted 12 October 2025

[3–7] or have focused on improving simulation performance through numerical optimization techniques. Examples include the semi-smooth Newton method [8], the deep backtracking algorithm [9], combinations with the arc-length method and under-relaxation schemes [10], the limited-memory quasi-Newton Broyden–Fletcher–Goldfarb–Shanno (BFGS) method [11], and the preconditioned inexact Newton method [12]. This study, however, adopts the latter strategy, focusing specifically on continuous methods.

Algorithmically optimized approaches within the continuous framework can generally be classified into large-scale (global) numerical optimization and material–point level (local) optimization. Large-scale optimization focuses on integrated systems, such as linearized equations, involving thousands of components. When optimizing such large physical systems, as discussed by Nocedal and Wright [13], the strategy includes (1) identifying objectives, (2) determining the characteristic variables of the physical system, and (3) finding solutions to optimize the physical system. For FEM-based fracture numerical analysis, the objective is typically the minimization of energy within the analyzed domain, as proposed by Francfort and Marigo [14], where the displacement fields are chosen as the basic characteristic variables. Several studies have successfully addressed robustness improvements for large-scale systems [11,15–18].

On the other hand, material–point level optimization focuses on the constituents of the large-scale physical system. These local optimizations play a crucial role in achieving global robustness [19,20], and the use of an algorithmic (consistent) tangent matrix enhances quadratic convergence [21]. Additionally, various constrained numerical optimization methods exist that offer good performance at the material-point level despite limitations for large-scale applications.

While researchers have focused on improving large-scale global robustness, these approaches are often inefficient and problem-dependent. This is particularly true when modeling combinations of complex constitutive material responses and heterogeneous FE models, such as polycrystalline materials within an anisotropic framework [22], steel alloys [23,24], and aluminum alloys [25]. In these cases, the crucial coupling between “single crystal plasticity” and “damage” significantly increases material instability. Physically, damage growth decreases the solid matrix volume fraction (representing the effective solid), which in turn enhances accumulated plastic slips. Consequently, “accurate” and “stable” global FE solutions to initial boundary value problems for ductile fracture materials cannot be expected if “inaccurate” and “unstable” state-update procedures are used.

Regarding spurious mesh-dependence and length scales, material fracture responses without mesh regularization often exhibit over-damaged phenomena [26–28], which can render global solutions impossible. To address this, a micromorphic-extended damage model was utilized in this study (for details, see [29–33]). The extra micromorphic variable, however, increased the physical system’s complexity due to scaling differences with standard displacements. Recently, Harandi et al. [34] proposed a practical similarity between micromorphic-extended and phase-field (PF) damage models. Because the micromorphic model contains a similar assembled stiffness matrix structure, globally unified approaches designed for the PF damage model can be directly inherited.

Regarding the coupling between micromorphic damage and single crystal plasticity, researchers have focused on strain-rate-dependent material modeling due to its superior numerical convergence compared to a rate-independent formulation. For instance, Sabnis et al. [35] proposed a two-surface ductile fracture model with normal stress damage criterion for slip planes to characterize plasticity-induced fracture in a Nickel-based superalloy, although it did not include stiffness-degradation from continuum damage mechanics (CDM). Ling et al. [36] and Scherer et al. [37] focused on micromorphic gradient-enhanced ductile fracture model based on the Gurson-Tvergaard-Needleman (GTN)-like porous single crystal plasticity [38–41], characterizing the microstructural texture effect on plasticity-dominant damage in single crystals. However, algorithmic optimization for polycrystals with strain-rate-independent crystal plasticity [42] and the brittle-to-ductile transition in multi-phase microstructures remain challenging.

Building upon these considerations, a novel stress-update algorithm with fully implicit integration is proposed for the micromorphic extended hyperelastic–single crystal plastic ductile solid material. This algorithm enhances local robustness. The key aspect of the designed algorithm lies in a natural separation between the plasticity and damage mechanisms under reasonable assumptions. The conventional multi-surface algorithm based on general CDM [43–47] can be significantly simplified into a sequential procedure without losing mathematical equivalence. This enables the analytical solution of damage evolution without requiring an internal nonlinear solver. The resulting sequential algorithm is more convenient for material modeling and requires less computational cost during polycrystalline ductile fracture simulation.

1.2. Structure of the present work

The remainder of this paper is organized as follows: Section 2 presents the constitutive material modeling formulations. This section details a systematic framework for single crystal plasticity coupled with micromorphic damage mechanics based on a rate-independent form, ensuring thermodynamic consistency. Section 3 provides an algorithmic discussion with a primary focus on local (material point level) aspects. A comparison between the conventional and proposed stress-update algorithms is emphasized, specifically highlighting the sequential procedure. Section 4 presents numerical examples across several applications, including mesh regularization, a discussion of factors influencing strain localization, and a comprehensive ductile fracture analysis within a polycrystalline material. Section 5 presents the conclusions. The verification of the proposed model and a discussion of its similarity with the PF damage model are provided in Appendix A.

2. Constitutive modeling and formulations

Building upon the work of Tan and Watanabe [33], this study constructed an extended model for ductile fracture constitutive modeling, from fundamental formulation to numerical implementation. To emphasize the algorithmic improvements within the polycrystalline material system, this section discusses only the essential formulations.

2.1. *Kinematics of finite strain elastoplastic damageable solid*

The deformation gradient $\mathbf{F}_t$ can be multiplicatively split into elastic $\mathbf{F}^{\mathrm{e}}$ and plastic $\mathbf{F}^{\mathrm{p}}$ components, as initially proposed by Lee [48] and applied to single crystal plasticity by Asaro [49]. This decomposition, which is commonly visualized in the plastic intermediate configuration, allows the kinematics of elastoplastic damageable materials to be expressed in terms of classical elastoplastic theory [50]. The decomposition is given by $\mathbf{F}_t = \mathbf{F}^{\mathrm{e}}\mathbf{F}^{\mathrm{p}}$. Here, $\boldsymbol{X}$ represents the position vector of the undeformed domain (reference configuration $\mathcal{R}_0$), which is a subset of the three-dimensional real space $\mathcal{R}$. The mapping $\varphi_{\mathrm{t}} : \mathcal{R}_0 \to \mathcal{R}_t$ describes the motion of the domain within the time interval $[0, \mathrm{T}]$, pushing forward the position vector $\boldsymbol{X}$ to the deformed position $\boldsymbol{x} = \varphi_t(\boldsymbol{X})$ in the current configuration $\mathcal{R}_t \subset \mathcal{R}$. The displacement is defined as $\mathbf{u}_t = \mathbf{x} - \mathbf{X}$, and the volumetric change is $J := \det\left(\mathbf{F}_t\right) > 0$. For simplicity, the subscript "t" is omitted in further formulations. Physically, these deformation gradients relate to different microscopic mechanisms. In single crystal plasticity, the plastic deformation gradient $\mathbf{F}^{\mathrm{p}}$ arises from the accumulation of inelastic slips on crystallographic slip systems, whereas the elastic deformation gradient $\mathbf{F}^{\mathrm{e}}$ accounts for the stretch and rotation of the crystal lattice. Accordingly, the condition of plastic incompressibility, $J^{\mathrm{p}} := \det(\mathbf{F}^{\mathrm{p}}) \equiv 1$, is assumed throughout this study.

2.2. *Consistent thermodynamic formulations*

To account for the complexities of ductile single crystal materials, a consistent thermodynamic formulation must be established. The second law of thermodynamics under isothermal conditions, expressed as ($W_0^{\mathrm{int}} - \rho\dot{\Psi} \geq 0$), describes the necessary relationship between the internal power density W_0^{int} in the reference configuration and the rate of Helmholtz free energy $\rho\dot{\Psi}$. This relationship can be expressed as:

$$\begin{aligned} W_0^{\mathrm{int}} - \rho\dot{\Psi} &= \mathbf{P} : \dot{\mathbf{F}} + a^{\mathrm{m}}\dot{\widetilde{\eta}} + \mathbf{b}^{\mathrm{m}} \cdot \nabla_{\boldsymbol{X}}\dot{\widetilde{\eta}} - \rho\dot{\Psi}\left(\mathbf{C}^{\mathrm{e}}, \widetilde{\eta}, \nabla_{\boldsymbol{X}}\widetilde{\eta}, \mathrm{D}, \boldsymbol{\xi}, \eta\right) \\ &= \mathbf{S} : \dot{\mathbf{E}} + a^{\mathrm{m}}\dot{\widetilde{\eta}} + \mathbf{b}^{\mathrm{m}} \cdot \nabla_{\boldsymbol{X}}\dot{\widetilde{\eta}} - \rho\left(2\frac{\partial\Psi}{\partial\mathbf{C}^{\mathrm{e}}} : \frac{1}{2}\dot{\mathbf{C}}^{\mathrm{e}} + \sum_{i=1}^{n_{\mathrm{slip}}}\frac{\partial\Psi}{\partial\xi^{(i)}}\dot{\xi}^{(i)} + \frac{\partial\Psi}{\partial\mathrm{D}}\dot{\mathrm{D}} + \frac{\partial\Psi}{\partial\eta}\dot{\eta} + \frac{\partial\Psi}{\partial\widetilde{\eta}}\dot{\widetilde{\eta}} + \frac{\partial\Psi}{\partial\nabla_{\boldsymbol{X}}\widetilde{\eta}} \cdot \nabla_{\boldsymbol{X}}\dot{\widetilde{\eta}}\right). \end{aligned} \tag{1}$$

According to Eq. (1), the internal power density is determined by the internal strain energy rate, which involves the 1st or 2nd Piola–Kirchhoff stress $\mathbf{P}$ or $\mathbf{S}$, and the Green–Lagrange strain tensor $\mathbf{E} = 1/2(\mathbf{F}^{\mathrm{T}}\mathbf{F} - \mathbf{I})$, where $\mathbf{I}$ is second-order identical tensor. It also involves two micromorphic resultants: the coupling force a^{m} and the micromorphic force $\mathbf{b}^{\mathrm{m}}$. The free energy is a time-dependent function of the elastic right Cauchy–Green tensor $\mathbf{C}^{\mathrm{e}} = \mathbf{F}^{\mathrm{e}\mathrm{T}}\mathbf{F}^{\mathrm{e}}$, micromorphic damage variable $\widetilde{\eta}$ and its gradient with respect to the reference configuration $\nabla_{\boldsymbol{X}}\widetilde{\eta}$, scalar damage variable D, and microscopic damage variable η. The series of microscopic plastic variables $\boldsymbol{\xi} = \{\xi^{(1)}, \dots, \xi^{(i)}\}$ describes the slip of the ith crystal slip system. The dependence of this quantity on the number of slip systems "n_{slip}" is a material property. To determine the full power–dissipation inequality, frame transformations of tensors are required (as detailed in previous work by Tan and Watanabe [33] and other textbooks). Furthermore, the free energy is assumed to be an additive expression: $\Psi = \Psi^{\mathrm{e}}(\mathbf{C}^{\mathrm{e}}, \mathrm{D}) + \Psi^{\mathrm{p}}(\boldsymbol{\xi}, \mathrm{D}) + \Psi^{\mathrm{d}}(\eta) + \Psi^{\mathrm{m}}\left(\eta, \widetilde{\eta}, \nabla_{\boldsymbol{X}}\widetilde{\eta}\right)$. Applying this to Eq. (1), the full Clausius–Duhem inequality is derived as:

$$\begin{aligned} &\left(\hat{\mathbf{S}} - 2\frac{\partial\Psi^{\mathrm{e}}}{\partial\mathbf{C}^{\mathrm{e}}}\right) : \dot{\mathbf{E}}^{\mathrm{e}} + \left(a^{\mathrm{m}} - \frac{\partial\Psi^{\mathrm{m}}}{\partial\widetilde{\eta}}\right)\dot{\widetilde{\eta}} + \left(\mathbf{b}^{\mathrm{m}} - \frac{\partial\Psi^{\mathrm{m}}}{\partial\nabla_{\boldsymbol{X}}\widetilde{\eta}}\right) \cdot \nabla_{\boldsymbol{X}}\dot{\widetilde{\eta}} \\ &\quad + \left(2\mathbf{C}^{\mathrm{e}}\frac{\partial\Psi^{\mathrm{e}}}{\partial\mathbf{C}^{\mathrm{e}}}\right) : \dot{\mathbf{F}}^{\mathrm{p}}\mathbf{F}^{\mathrm{p}-1} - \sum_{i=1}^{n_{\mathrm{slip}}}\frac{\partial\Psi^{\mathrm{p}}}{\partial\xi^{(i)}}\dot{\xi}^{(i)} + \left(-\frac{\partial(\Psi^{\mathrm{e}} + \Psi^{\mathrm{p}})}{\partial\mathrm{D}}\right)\dot{\mathrm{D}} - \frac{\partial\left(\Psi^{\mathrm{d}} + \Psi^{\mathrm{m}}\right)}{\partial\eta}\dot{\eta} \qquad \geqslant 0, \end{aligned} \tag{2}$$

where $\hat{\mathbf{S}}$ and $\mathbf{E}^{\mathrm{e}} = 1/2(\mathbf{C}^{\mathrm{e}} - \mathbf{I})$ are the second Piola–Kirchhoff stress tensor and the elastic Green–Lagrange strain in the intermediate configuration, respectively. In Eq. (2), the micromorphic damage coupling term $a^{\mathrm{m}}\dot{\widetilde{\eta}}$ and gradient term $\mathbf{b}^{\mathrm{m}} \cdot \nabla_{\boldsymbol{X}}\dot{\widetilde{\eta}}$ are assumed to be purely energetic conjugate forces, as discussed in the literature on gradient-enhanced material modeling [51–53]. Applying the standard Coleman–Noll procedure yields the reduced dissipation inequality $\mathcal{D}$:

$$\mathcal{D} := \hat{\mathbf{M}} : \mathbf{L}^{\mathrm{p}} - \sum_{i=1}^{n_{\mathrm{slip}}}\left(\tau_{\mathrm{c}}^{(i)}\dot{\xi}^{(i)}\right) + Y^{\mathrm{d}}\dot{\mathrm{D}} - \beta\dot{\eta} \geqslant 0. \tag{3}$$

Additionally, the following thermodynamic conjugate forces are derived:

$$\hat{\mathbf{S}} = 2\frac{\partial\Psi^{\mathrm{e}}}{\partial\mathbf{C}^{\mathrm{e}}};\ \ \tau_{\mathrm{c}}^{(i)} = \frac{\partial\Psi^{\mathrm{p}}}{\partial\xi^{(i)}};\ \ \hat{\mathbf{M}} = \mathbf{C}^{\mathrm{e}}\hat{\mathbf{S}};\ \ \mathbf{L}^{\mathrm{p}} = \dot{\mathbf{F}}^{\mathrm{p}}\mathbf{F}^{\mathrm{p}-1}; a^{\mathrm{m}} = \frac{\partial\Psi^{\mathrm{m}}}{\partial\widetilde{\eta}};\ \ Y^{\mathrm{d}} = -\frac{\partial(\Psi^{\mathrm{e}} + \Psi^{\mathrm{p}})}{\partial\mathrm{D}};\ \ \mathbf{b}^{\mathrm{m}} = \frac{\partial\Psi^{\mathrm{m}}}{\partial\nabla_{\boldsymbol{X}}\widetilde{\eta}};\ \ \beta = \beta^{\mathrm{d}} + \beta^{\mathrm{m}} = \frac{\partial\Psi^{\mathrm{d}}}{\partial\eta} + \frac{\partial\Psi^{\mathrm{m}}}{\partial\eta}. \tag{4}$$

The elastoplastic state, defined on the plastic intermediate configuration, includes the second Piola–Kirchhoff stress $\hat{\mathbf{S}}$, the unsymmetric elastic Mandel stress $\hat{\mathbf{M}}$, and the plastic velocity gradient $\mathbf{L}^{\mathrm{p}}$. The components also include the isothermal plastic resistance of the ith slip system $\tau_{\mathrm{c}}^{(i)}$, which describes the statistical microscopic plastic mechanism. The damage components consist of the damage norm (or energy release rate) Y^{d}, conjugated to the damage variable D, and the specific microscopic damage resistance β, which is conjugated to the damage variable η and includes a micromorphic contribution β^{m}. These general expressions demonstrate theoretical consistency for the coupling between single crystal plasticity and damage mechanisms.

2.3. Evolution of internal state variables

To satisfy the reduced energy-dissipation inequality from Eq. (3), a local optimization is applied to this plasticity–damage coupling system. This approach assumes a relationship between effective quantities and their undamaged counterparts $(\bullet)^*$, such as $\mathbf{S}^* = \mathbf{S}/f(\mathrm{D})$, based on the hypothesis of strain equivalence [46]. The degradation function $f(\mathrm{D})$ represents the volume fraction of the solid part. The Lagrangian multiplier method is applied to maximize the plasticity–damage reduced dissipation with constraints related to the plasticity $\phi^{\mathrm{p}(i)}$ and the micromorphic damage ϕ^{m}. For a detailed discussion on local inequality satisfaction, we refer to Nocedal and Wright [13]. The Lagrangian is defined as:

$$\mathcal{L} = -\mathcal{D}\left(\hat{\mathbf{M}}, \boldsymbol{\tau}_{\mathrm{c}}, Y^{\mathrm{d}}, \beta\right) + \sum_{i=1}^{n_{\mathrm{slip}}} \gamma_{\mathrm{p}}^{(i)} \phi^{\mathrm{p}(i)} + \gamma_{\mathrm{d}} \phi^{\mathrm{m}}, \tag{5}$$

where $\gamma_{\mathrm{p}} = \{\gamma_{\mathrm{p}}^{(1)}, \dots, \gamma_{\mathrm{p}}^{(i)}\}$ and γ_{d} are the multipliers. The yield function $\phi^{\mathrm{p}(i)}$ of the ith slip system, which serves as the constraint for plasticity, is defined as:

$$\phi^{\mathrm{p}(i)} = |\tau_{\mathrm{r}}^{(i)}| - \tau_{\mathrm{c}}^{(i)} = f(\mathrm{D})|\tau_{\mathrm{r}}^{(i)*}| - h(\mathrm{D})\tau_{\mathrm{c}}^{(i)*} \leq 0, \tag{6}$$

where $|\tau_{\mathrm{r}}^{(i)}|$ is the non-signed resolved shear stress on the ith slip system. The micromorphic damage criterion is:

$$\phi^{\mathrm{m}} = Y^{\mathrm{d}} - \beta \leq 0. \tag{7}$$

Based on Eqs. (5) to (7), the Karush–Kuhn–Tucker (KKT) conditions are defined as:

$$\gamma_{\mathrm{p}}^{(i)} \geqslant 0, \quad \phi^{\mathrm{p}(i)} \leqslant 0, \quad \gamma_{\mathrm{p}}^{(i)} \phi^{\mathrm{p}(i)} = 0 \quad \forall i \in \left\{1, \dots, n_{\mathrm{slip}}\right\}, \tag{8}$$

$$\gamma_{\mathrm{d}} \geqslant 0, \quad \phi^{\mathrm{m}} \leqslant 0, \quad \gamma_{\mathrm{d}} \phi^{\mathrm{m}} = 0. \tag{9}$$

For numerical stability, a Perzyna-like strain-rate-dependent term Q is appended to Eq. (6). The full plastic criterion is therefore given by:

$$\phi^{\mathrm{p}(i)} = |\tau_{\mathrm{r}}^{(i)}| - \tau_{\mathrm{c}}^{(i)} Q\left(\Delta\gamma_{\mathrm{p}}^{(i)}\right) = f(\mathrm{D})|\tau_{\mathrm{r}}^{(i)*}| - h(\mathrm{D})\tau_{\mathrm{c}}^{(i)*} Q\left(\Delta\gamma_{\mathrm{p}}^{(i)}\right) \leq 0. \tag{10}$$

$$Q\left(\Delta\gamma_{\mathrm{p}}^{(i)}\right) = \left(r_{\mathrm{b}} \frac{\Delta\gamma_{\mathrm{p}}^{(i)}}{\Delta t} + 1\right)^{r_{\mathrm{a}}}, \tag{11}$$

where r_{a} and r_{b} are material constants for the strain-rate-dependency and $\Delta t = t_{\mathrm{n+1}} - t_{\mathrm{n}}$ is a discretized time interval between incremental steps. Also, the time-discretized Lagrangian multiplier of ith slip system is defined as $\Delta\gamma_{\mathrm{p}}^{(i)} = \Delta t \gamma_{\mathrm{p}}^{(i)}$. This appended term is not intended to model creep behavior, but rather to improve the stability of strain-rate-independent single crystal plasticity, as discussed by Miehe [42], Peirce et al. [54], and Miehe and Schröder [55].

By applying the stationarity condition (maximum) to the Lagrangian function $\mathcal{L}$, the evolution equations for all internal variables are derived. The evolution of plastic resultants is obtained from the directional variations:

$$\begin{aligned} &\frac{\partial \mathcal{L}}{\partial \hat{\mathbf{M}}} = \mathbf{0} \Rightarrow \mathbf{L}^{\mathrm{p}} = \sum_{i=1}^{n_{\mathrm{slip}}} \gamma_{\mathrm{p}}^{(i)} \mathbf{N}^{\mathrm{p}(i)} \operatorname{sign}\left(\tau_{\mathrm{r}}^{(i)}\right); \\ &\mathbf{N}^{\mathrm{p}(i)} = \frac{\partial \phi^{\mathrm{p}(i)}}{\partial \hat{\mathbf{M}}}; \end{aligned} \tag{12}$$

$$\frac{\partial \mathcal{L}}{\partial \tau_{\mathrm{c}}^{(i)}} = 0 \quad \forall i \in \left\{1, \dots, n_{\mathrm{slip}}\right\} \quad \Rightarrow \dot{\xi}^{(i)} = \gamma_{\mathrm{p}}^{(i)} Q\left(\Delta\gamma_{\mathrm{p}}^{(i)}\right). \tag{13}$$

The plastic flow $\mathbf{L}^{\mathrm{p}}$ is defined as the integration of all slips. The damage evolutions are as follows:

$$\frac{\partial \mathcal{L}}{\partial Y^{\mathrm{d}}} = 0 \Rightarrow \dot{\mathrm{D}} = \gamma_{\mathrm{d}}; \qquad \frac{\partial \mathcal{L}}{\partial \beta} = 0 \Rightarrow \dot{\eta} = \gamma_{\mathrm{d}}; \tag{14}$$

Here, the evolution for the two damage variables, D and η, is identical, implying that these variables are identical if their initial values are the same. Using the elastic and plastic degradation functions, $f(\mathrm{D})$ and $h(\mathrm{D})$, the plastic and damage norms, derived from Eq. (4), can be rewritten as:

$$\begin{aligned} &\tau_{\mathrm{r}}^{(i)} = f(\mathrm{D}) \hat{\mathbf{M}}^* : \mathbf{N}^{\mathrm{p}(i)}; \\ &Y^{\mathrm{d}} = -\left(\frac{\partial f(\mathrm{D})}{\partial \mathrm{D}} \Psi^{\mathrm{e}*} + \frac{\partial h(\mathrm{D})}{\partial \mathrm{D}} \Psi^{\mathrm{p}*}\right). \end{aligned} \tag{15}$$

The micromorphic damage criterion ϕ^{m} can be further derived to express damage regularization via the global micromorphic balance [30,33] by replacing the coupling relation of the extra damage hardening term β^{m}:

$$\phi^{\mathrm{m}} = Y^{\mathrm{d}} - \left(\beta^{\mathrm{d}} - \nabla_{\boldsymbol{X}} \cdot \mathbf{b}^{\mathrm{m}}\right). \tag{16}$$

Here, the last term of the extended criterion serves as an additional source due to the damage mechanism, which describes a phenomenon proportional to the Laplacian of micromorphic damage objects (voids and cracks) $\widetilde{\eta}$.

2.4. *Definitions of the Helmholtz free energy*

The proposed constitutive model for finite strain elastoplastic damageable material is sufficiently general, despite certain assumptions. In practice, specific Helmholtz free energies must be defined to capture different material responses.

An undamaged St.Venant hyperelastic quadratic energy $\Psi^{\mathrm{e}*}$ is chosen for general anisotropic elasticity, with quantities defined on the intermediate configuration:

$$\Psi^{\mathrm{e}*} = \frac{1}{2}\,\mathbf{E}^{\mathrm{e}} : \hat{\mathbb{C}}^{\mathrm{e}} : \mathbf{E}^{\mathrm{e}}. \tag{17}$$

The fourth-order elastic modulus $\hat{\mathbb{C}}^{\mathrm{e}}$ is mapped from the crystal lattice configuration to an initial specimen configuration using the crystallographic orientation. Additionally, the undamaged single crystal plastic potential energy $\Psi^{\mathrm{p}*}$ is chosen in a mixed form:

$$\Psi^{\mathrm{p}*} = \sum_{k=1}^{N}\left[\sum_{i=1}^{kn_{\mathrm{slip}}}\xi^{(i)}\left(\tau_0^{(k)} + H^{\mathrm{p}(k)}\sum_{j=1}^{n_{\mathrm{slip}}}\frac{1}{2}\Omega_{ij}^{(k)}\xi^{(j)} + \delta\tau_{\mathrm{s}}^{(k)}\right) + \frac{\left(\delta\tau_{\mathrm{s}}^{(k)}\right)^2}{h^{\mathrm{p}(k)}}\left(\exp\left[-\frac{h^{\mathrm{p}(k)}}{\delta\tau_{\mathrm{s}}^{(k)}}\sum_{i=1}^{kn_{\mathrm{slip}}}\xi^{(i)}\right] - 1\right)\right], \tag{18}$$

where $\tau_0^{(k)}$, $H^{\mathrm{p}(k)}$, $\Omega_{ij}^{(k)}$, $\delta\tau_{\mathrm{s}}^{(k)}$, and $h^{\mathrm{p}(k)}$ are material constants for single crystal plasticity. N and kn_{slip} are the numbers of slip system set and slip systems in kth slip set, respectively. For instance, a face-centered cubic (FCC) system has one slip system set with 12 slip systems, while a body-centered cubic (BCC) system has three slip system sets with a total of 48 slip systems. Based on the definitions in Eq. (4), expressions for the second Piola–Kirchhoff stress $\hat{\mathbf{S}}$ and the isothermal plastic resistance $\tau_{\mathrm{c}}^{(i)}$ of ith slip system are derived:

$$\hat{\mathbf{S}} = f(\mathrm{D})\hat{\mathbf{S}}^* = f(\mathrm{D})\hat{\mathbb{C}}^{\mathrm{e}} : \mathbf{E}^{\mathrm{e}}; \tag{19}$$

$$\tau_{\mathrm{c}}^{(i)} = h(\mathrm{D})\tau_{\mathrm{c}}^{*(i)} = h(\mathrm{D})\left\{\tau_0^{(i)} + H^{\mathrm{p}(i)}\sum_{j=1}^{n_{\mathrm{slip}}}\Omega_{ij}^{(i)}\xi^{(j)} + \delta\tau_{\mathrm{s}}^{(i)}\left(1 - \exp\left[-\frac{h^{\mathrm{p}(i)}}{\delta\tau_{\mathrm{s}}^{(i)}}\sum_{j=1}^{n_{\mathrm{slip}}}\xi^{(j)}\right]\right)\right\}. \tag{20}$$

According to Eq. (20), the critical resolved shear stress (CRSS) for the ith slip system, $\tau_{\mathrm{c}}^{*(i)}$, includes initial CRSS $\tau_0^{(k)}$, linear hardening modulus $H^{\mathrm{p}(k)}$, interaction matrix $\Omega_{ij}^{(k)}$, and Voce-type nonlinear hardening parameters $\delta\tau_{\mathrm{s}}^{(k)}$ and $h^{\mathrm{p}(k)}$. For this study, the interaction matrix is simplified to model self- and latent-hardening systems, where $\Omega_{ii}^{(k)} = 1$ and $\Omega_{ij}^{(k)}$ $(i \neq j)$.

The resolved shear stress, as the stress norm defined in Eqs. (10) and (15), is given by:

$$\tau_{\mathrm{r}}^{(i)} = f(\mathrm{D})\hat{\mathbf{M}}^* : \left(\boldsymbol{s}_0^{(i)} \otimes \boldsymbol{m}_0^{(i)}\right), \tag{21}$$

where the slip direction vector $\boldsymbol{s}_0^{(i)}$ and the normal vector of the slip plane $\boldsymbol{m}_0^{(i)}$ for the ith slip system are defined at the intermediate configuration. Because no lattice rotation occurs during slip deformation, these vectors are identical to those at the initial configuration. They are mapped from the base vectors of the crystal lattice configuration based on the crystallographic orientations. Furthermore, a push-forward operation maps them to the deformed configuration using the elastic deformation gradient:

$$\boldsymbol{s}^{(i)} = \mathbf{F}^{\mathrm{e}}\boldsymbol{s}_0^{(i)}; \quad \boldsymbol{m}^{(i)} = \mathbf{F}^{\mathrm{e}-\mathrm{T}}\boldsymbol{m}_0^{(i)}; \tag{22}$$

Following Eqs. (15) and (21), the plastic flow directional tensor of ith slip system is $\mathbf{N}^{\mathrm{p}(i)} := \boldsymbol{s}_0^{(i)} \otimes \boldsymbol{m}_0^{(i)}$, which describes the crystallographic anisotropy in plasticity and is known as the Schmid tensor.

The damage potential energy Ψ^{d} is defined for the isotropic damage hardening β^{d}:

$$\Psi^{\mathrm{d}} = \Psi_0^{\mathrm{d}}(1 - \exp[-\eta]) + H^{\mathrm{d}}(1 - \exp[-\eta] - \eta\exp[-\eta]). \tag{23}$$

This free energy term must satisfy the requirements that $\Psi^{\mathrm{d}} = 0$ and $(\Psi^{\mathrm{d}})' = \Psi_0^{\mathrm{d}}$ when $\eta = 0$. It includes two material constants: the damage energy threshold Ψ_0^{d} and the damage hardening modulus H^{d}.

The micromorphic damage energy Ψ^{m} is defined for the micromorphic damage hardening on the reference configuration via coupling and gradient terms. Notably, it is utilized to express the extra damage-growth mechanism due to micromorphic extension in Eq. (26), and is verified within Appendix A.

$$\Psi^{\mathrm{m}} = H^{\mathrm{m}}\left(1 - \exp\left[\widetilde{\eta} - \eta\right] - \left(\eta - \widetilde{\eta}\right)\exp\left[\widetilde{\eta} - \eta\right]\right) + \frac{1}{2}\nabla_{\boldsymbol{X}}\widetilde{\eta}\cdot\boldsymbol{A}\cdot\nabla_{\boldsymbol{X}}\widetilde{\eta}. \tag{24}$$

Here, the second-order tensor $\boldsymbol{A}$ represents the general anisotropic micromorphic modulus. The definition within Eq. (4) leads to the damage hardening β^{d}, micromorphic damage hardening β^{m}, coupling term a^{m}, and micromorphic gradient term $\mathbf{b}^{\mathrm{m}}$ in the reference configuration, as follows:

$$\beta^{\mathrm{d}} = \exp[-\eta]\left(\Psi_0^{\mathrm{d}} + H^{\mathrm{d}}\eta\right); \quad \beta^{\mathrm{m}} = \exp\left[\widetilde{\eta} - \eta\right]H^{\mathrm{m}}\left(\eta - \widetilde{\eta}\right); \tag{25}$$

$$a^{\mathrm{m}} = \exp\left[\widetilde{\eta} - \eta\right]H^{\mathrm{m}}\left(\widetilde{\eta} - \eta\right); \tag{26}$$

$$\mathbf{b}^{\mathrm{m}} = \boldsymbol{A}\cdot\nabla_{\boldsymbol{X}}\widetilde{\eta} \underset{\text{condition}}{\overset{\text{isotropic}}{\Longrightarrow}} A^{\mathrm{m}}\nabla_{\boldsymbol{X}}\widetilde{\eta}. \tag{27}$$

where H^{m} and A^{m} are the coupling and micromorphic moduli, respectively.

The functions $f(\mathrm{D})$ and $h(\mathrm{D})$ are the elastic and plastic degradation functions, respectively. They are not necessarily the same and are utilized to express the shape of damage growth zones:

$$f(\mathrm{D}) = \exp[-\mathrm{D}], \qquad h(\mathrm{D}) = 1 - \alpha(1 - \exp[-\mathrm{D}]), \tag{28}$$

where α is a control parameter for elastic and plastic contributions, and in this study, it is set to $\alpha = 1$ to enable the subsequent sequential algorithm. The damage criterion in Eq. (7) can then be expressed as:

$$\phi^{\mathrm{m}} = Y^{\mathrm{d}} - \beta = \exp[-\mathrm{D}]\left(\Psi^{\mathrm{e}*} + \alpha\Psi^{\mathrm{p}*}\right) - \exp[-\eta]\left(\Psi_0^{\mathrm{d}} + H^{\mathrm{d}}\eta + H^{\mathrm{m}}\exp\left[\tilde{\eta}\right]\left(\eta - \tilde{\eta}\right)\right). \tag{29}$$

Further analysis is performed to achieve global micromorphic balance with the characteristic length l_{c}. The familiar gradient form is derived as follows:

$$\begin{cases} \tilde{\eta} - l_{\mathrm{c}}^2 \nabla_{\boldsymbol{X}}^2 \tilde{\eta} = \eta \qquad \forall \boldsymbol{X} \in \Omega_0; \\ l_{\mathrm{c}} := \sqrt{\dfrac{A^{\mathrm{m}}}{H^{\mathrm{m}}\exp\left[\tilde{\eta} - \eta\right]}}; \end{cases} \tag{30}$$

This term is derived as a regularized object in the micromorphic extended damage model.

A complete explanation of the general and decoupled damageable solid is provided in Fig. 1, where $(\bullet)^{\mathrm{M}}$ and $(\bullet)^{\mathrm{m}}$ represent macroscopic and microscopic resultants, respectively, following the conventional homogenization theory in Watanabe et al. [56]. Within this framework, the microscopic aspects of the damageable single crystal plastic material with $\boldsymbol{\xi} = \{\xi^1, \ldots, \xi^{(i)}\}$ and the micromorphic extended damage material with η and $\tilde{\eta}$ are demonstrated. In general, the plasticity is strongly coupled with the damage, which is mathematically represented by the local coupling between plasticity and damage potentials (ϕ^{p}–ϕ^{m}). Accordingly, various material constitutive responses can define the parameters τ_{c} and τ_{r} for plasticity, Y^{d}, β^{d}, β^{m} and $\mathbf{b}^{\mathrm{m}}$ for damage. According to the conventional case (the left side of Fig. 1) proposed by Tan and Watanabe [33], the two micromorphic terms, $\beta^{\mathrm{m}}(\eta - \tilde{\eta})$ and $a^{\mathrm{m}}(\eta - \tilde{\eta})$, express the length scale of microscopic damage zones induced by the coupling between the two damage variables. These terms are assumed to be zero within the PF damage theory, which characterizes a two-dimensional crack surface.

The proposed material model, which follows the sequential scheme (the right side of Fig. 1), is considered a special case, particularly for crystal plasticity–ductile damage. Using a suitable effective solid definition, where $f(\mathrm{D}) \equiv h(\mathrm{D})$ (and the undamaged quantity is denoted by $(\bullet)^*$), the conventional plasticity–damage coupling can be reduced to a decoupled material model and thus leads to a transition from (ϕ^{p}–ϕ^{m}) to ($f(\mathrm{D})\phi^{\mathrm{p}*}$–$\phi^{\mathrm{m}}$). Examples of these functions include the linear form in Lemaitre [46], the quadratic form proposed by Brepols et al. [32], and the exponential form in Eq. (28) with ($\alpha = 1$). Owing to the fully implicit material time integration, the micromorphic damage term $\beta^{\mathrm{d+m}}$ is proposed to characterize the same damage mechanism. For instance, the definitions in Eqs. (25) to (28) are reduced to the same block $\exp[-\eta]\beta^{(\mathrm{d+m})*}$, which includes damage and micromorphic extension in Fig. 1. Additionally, this coupling can be further simplified to $f(\mathrm{D})(\phi^{\mathrm{p}*}$–$\phi^{\mathrm{m}*})$ using the evolution equations in Eq. (14). An analytical solution for the damage variables can be derived from Eqs. (4), (7), (25)–(28) without requiring an internal nonlinear solver. Finally, the proposed sequential plasticity–damage coupling $f(\mathrm{D})(\phi^{\mathrm{p}*} \to \phi^{\mathrm{m}*})$ is obtained with a “one-pass” through the undamaged total elastoplastic energy $\Psi^{\mathrm{total}*}$.

The sequential algorithm structure is similar to the “divide–conquer” strategy, with inelastic internal state variables updated simultaneously under implicit integration. The numerical solutions between modeling frameworks should be consistent, differing only in algorithmic robustness in complex systems. The “staggered” approach in PF damage simulations performed by Miehe et al. [57,58] has been shown to produce inconsistent results with monolithic frameworks for large time increments; however, these inconsistencies can be mitigated by introducing extra criteria [59,60], albeit with increased computational cost.

3. Implicit algorithmic improvement

This section discusses the algorithmic aspects. The numerically implemented method is based on the finite element method (FEM). First, the global FE structure is reviewed, and then, as the key contribution, we propose a novel stress-update algorithm, which is the sequential plasticity–damage algorithm illustrated on the right side of the framework in Fig. 1. Two crucial verifications are provided in the Appendices: Appendix A provides details on constitutive similarity with the PF damage model and the proposed micromorphic damage mechanisms, and Appendix B demonstrates mathematical equivalence with the conventional algorithm.

The global FE procedure, discussed in a previous work [33], is implemented within the Multi-physics Object-Oriented Simulation Environment (MOOSE) [61]. The global linear momentum equilibrium is implemented within the total Lagrange framework (reference configuration), utilizing the second Piola–Kirchhoff stress $\mathbf{S}$ with the total Cauchy–Lagrange strain $\mathbf{E}$, the coupling force a^{m} with the scalar term $\tilde{\eta}$, and the micromorphic force $\mathbf{b}^{\mathrm{m}}$ with the gradient term $\nabla_{\boldsymbol{X}}\tilde{\eta}$.

The global coupled residuals $\mathrm{r} = \left\{\mathrm{r}^{\mathrm{u}}, \mathrm{r}^{\tilde{\eta}}\right\}^{\mathrm{T}}$ can be defined by applying the virtual-work principle to satisfy the balance equations. This FE discretization is considered a two-field coupled form, including the nodal displacement vector field $\mathbf{d}^{\mathrm{u}}$ and micromorphic scalar field $\mathbf{d}^{\tilde{\eta}}$ with test and trial components. Within fracture analysis, this FE system is nonlinear, both materially and geometrically; therefore, suitable time-integration and linearization methods are required for calculating the incremental $\Delta\mathbf{d}^{\mathrm{u}}$ and $\Delta\mathbf{d}^{\tilde{\eta}}$. The fully implicit Euler method is used for time-incremental steps, and the standard Newton method for nonlinear iterative steps. Within the Newton iteration of a time step ($t_{\mathrm{n+1}}$), current coupled residuals $(\mathrm{r})_{(\mathrm{n+1})(t_{\mathrm{n+1}})}$ and the Jacobian matrix $(\mathrm{K})_{(\mathrm{n+1})(t_{\mathrm{n+1}})}$ after linearization are supplied to the linear solver. Owing to this global framework, these ingredients must be updated during each global nonlinear

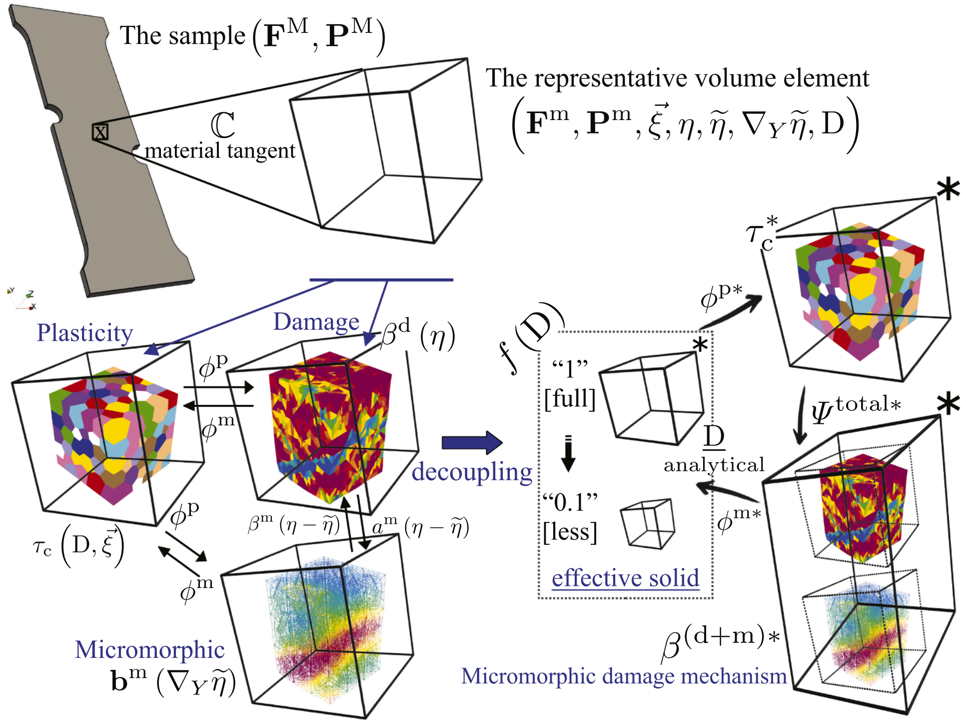

Fig. 1. Schematic of the implicit framework for modeling damageable materials. The left side presents the general material model, as described in [33]. The right side illustrates its reduction to a sequential scheme. The sequential scheme is achieved by applying the decoupling assumptions, specifically $\alpha = 1$ and the micromorphic damage mechanism in Eqs. (23) and (24)..

iteration, with the linearized equation of the coupled problem defined as follows:

$$\left[(\mathbb{K})_{(n+1)(t_{n+1})}\right]\begin{Bmatrix}\Delta\mathbf{d}^{u}\\ \Delta\mathbf{d}^{\widetilde{\eta}}\end{Bmatrix}_{(n+1)(t_{n+1})} = -(\mathbb{r})_{(n)(t_{n+1})}. \tag{31}$$

The global time-integration and nonlinear framework discussed previously plays a key role in improving robust convergence and subtly affects algorithmic design at the material point level.

3.1. Local aspect: the plasticity–damage coupling algorithm

As discussed in Section 2.3, a fully implicit stress-update algorithm was derived for the proposed model. This algorithm uses a general exponential mapping for plasticity and scalar backward Euler integration for damage. The verification is provided in Appendix B.

3.1.1. Incremental form of constitutive model

The global time interval $[0, \mathrm{T}]$ of interest can be integrated by subintervals. We will focus on a typical subinterval $[t_{\mathrm{n}}, t_{\mathrm{n+1}}]$. The time interval can be controlled by a cutting parameter θ, where $\mathbf{t} := t_{\mathrm{n}} + \theta\Delta t$ and $0 \le \theta \le 1$. Suppose that the total deformation gradient $\mathbf{F}_{\mathrm{t}}$, the micromorphic damage variable $\widetilde{\eta}_{\mathrm{t}}$ and its gradients $\nabla_{\boldsymbol{X}}\widetilde{\eta}_{\mathrm{t}}$ are prescribed. Assume also that state-dependent variables from the prior global time-incremental step, including the plastic deformation gradient $\mathbf{F}^{\mathrm{p}}_{t_{\mathrm{n}}}$, the plastic variables $\{\xi^{(1)}_{t_{\mathrm{n}}}, \ldots, \xi^{(n_{\mathrm{slip}})}_{t_{\mathrm{n}}}\}$, the damage variable $\mathrm{D}_{t_{\mathrm{n}}}$, and the microscopic damage variable $\eta_{t_{\mathrm{n}}}$, are known. Based on a formulation for strain-rate-independent single crystal plasticity [21,50]), the evolution Eqs. (12) and (14) and KKT conditions (8) and (9) are rewritten in a time-discretized incremental form:

$$\dot{\mathbf{F}}^{\mathrm{p}} = \left(\sum_{i=1}^{n_{\mathrm{slip}}} \gamma_{\mathrm{p}}^{(i)} \mathbf{N}^{\mathrm{p}(i)} \mathrm{sign}\left(\tau_{\mathrm{r}}^{(i)}\right)\right)\mathbf{F}^{\mathrm{p}} \Rightarrow \mathbf{F}^{\mathrm{p}}_{\mathrm{t}} = \exp\left[\sum_{i=1}^{n_{\mathrm{slip}}} \left(\Delta\gamma_{\mathrm{p}}^{(i)}\right)_{\mathrm{t}} \mathbf{N}^{\mathrm{p}(i)} \mathrm{sign}\left(\tau_{\mathrm{r}}^{(i)}\right)\right]\mathbf{F}^{\mathrm{p}}_{t_{\mathrm{n}}}. \tag{32}$$

$$\xi_{\mathrm{t}}^{(i)} = \xi_{t_{\mathrm{n}}}^{(i)} + \left(\Delta\gamma_{\mathrm{p}}^{(i)} Q\left(\Delta\gamma_{\mathrm{p}}^{(i)}\right)\right)_{\mathrm{t}} \quad \forall i \in \left\{1, \ldots, n_{\mathrm{slip}}\right\}; \tag{33}$$

$$\mathrm{D}_{\mathrm{t}} = \mathrm{D}_{t_{\mathrm{n}}} + \left(\Delta\gamma_{\mathrm{d}}\right)_{\mathrm{t}}; \quad \eta_{\mathrm{t}} = \eta_{t_{\mathrm{n}}} + \left(\Delta\gamma_{\mathrm{d}}\right)_{\mathrm{t}}. \tag{34}$$

$$\left(\Delta\gamma_{\mathrm{p}}^{(i)}\right)_{\mathrm{t}} \geqslant 0, \quad \phi^{\mathrm{p}(i)} \leqslant 0, \quad \left(\Delta\gamma_{\mathrm{p}}^{(i)}\right)_{\mathrm{t}} \phi^{\mathrm{p}(i)} = 0 \quad \forall i \in \left\{1, \ldots, n_{\mathrm{slip}}\right\}; \tag{35}$$

$$\left(\Delta\gamma_{\mathrm{d}}\right)_{\mathfrak{t}} \geqslant 0, \quad \phi^{\mathrm{m}} \leqslant 0, \quad \left(\Delta\gamma_{\mathrm{d}}\right)_{\mathfrak{t}}\phi^{\mathrm{m}} = 0. \tag{36}$$

In the state-update algorithm, the multipliers $\boldsymbol{\Delta\gamma}_{\mathrm{p}}$ and $\Delta\gamma_{\mathrm{d}}$ are found using a numerical iterative method to satisfy the following plastic and damage criteria for the active set of plastic and damage multipliers, $\mathcal{A}_{\mathrm{act}}$:

$$\phi^{\mathrm{p}(i)} = \left|\hat{\mathbf{M}} : \left\{\boldsymbol{s}_0^{(i)} \otimes \boldsymbol{m}_0^{(i)}\right\}\right| - \tau_{\mathrm{c}}^{(i)} = 0, \tag{37}$$

$$\phi^{\mathrm{m}} = \exp[-\mathrm{D}]\left(\Psi^{\mathrm{e}*} + \alpha\Psi^{\mathrm{p}*}\right) - \left(\beta^{\mathrm{d}} + \beta^{\mathrm{m}}\right) = 0. \tag{38}$$

3.1.2. *Implicit stress-update algorithm in the conventional approach*

The linearized interior system is derived from the global finite element nonlinear system. In this context, $\mathfrak{t}$, n, and k denote the global time increment, the global nonlinear iteration, and the interior nonlinear iteration, respectively. This system is used to solve for the time-discretized incremental multipliars $\Delta(\Delta\gamma_{\mathrm{p}}^{(i)})$ and $\Delta(\Delta\gamma_{\mathrm{d}})$. In the general case of polycrystalline ductile fracture, this system is highly nonlinear and strongly affects the global Jacobian matrix $(\mathbb{K})_{(\mathrm{n}+1)(\mathfrak{t}_{\mathrm{n}+1})}$ in Eq. (31), which presents the main challenge to achieving a robust solution.

$$\left(\begin{bmatrix} \dfrac{\mathrm{d}\phi^{\mathrm{p}(1)}}{\mathrm{d}\Delta\gamma_{\mathrm{p}}^{(1)}} & \cdots & \dfrac{\mathrm{d}\phi^{\mathrm{p}(1)}}{\mathrm{d}\Delta\gamma_{\mathrm{p}}^{(i)}} & \dfrac{\mathrm{d}\phi^{\mathrm{p}(1)}}{\mathrm{d}\Delta\gamma_{\mathrm{d}}} \\ \cdots & \cdots & \cdots & \cdots \\ \dfrac{\mathrm{d}\phi^{\mathrm{p}(i)}}{\mathrm{d}\Delta\gamma_{\mathrm{p}}^{(1)}} & \cdots & \dfrac{\mathrm{d}\phi^{\mathrm{p}(i)}}{\mathrm{d}\Delta\gamma_{\mathrm{p}}^{(i)}} & \dfrac{\mathrm{d}\phi^{\mathrm{p}(i)}}{\mathrm{d}\Delta\gamma_{\mathrm{d}}} \\ \dfrac{\mathrm{d}\phi^{\mathrm{m}}}{\mathrm{d}\Delta\gamma_{\mathrm{p}}^{(1)}} & \cdots & \dfrac{\mathrm{d}\phi^{\mathrm{m}}}{\mathrm{d}\Delta\gamma_{\mathrm{p}}^{(i)}} & \dfrac{\mathrm{d}\phi^{\mathrm{m}}}{\mathrm{d}\Delta\gamma_{\mathrm{d}}} \end{bmatrix}^{k} \begin{Bmatrix} \Delta\left(\Delta\gamma_{\mathrm{p}}^{(1)}\right) \\ \cdots \\ \Delta\left(\Delta\gamma_{\mathrm{p}}^{(i)}\right) \\ \Delta\left(\Delta\gamma_{\mathrm{d}}\right) \end{Bmatrix}^{k+1} = -\begin{Bmatrix} \phi^{\mathrm{p}(1)} \\ \cdots \\ \phi^{\mathrm{p}(i)} \\ \phi^{\mathrm{m}} \end{Bmatrix}^{k}\right)_{(\mathrm{n}+1)(\mathfrak{t}).} \tag{39}$$

If the Jacobian matrix $\mathrm{d}\phi/\mathrm{d}\boldsymbol{\Delta\gamma}$ is singular, a unique solution cannot be obtained. Following investigations of this linear algebraic equation [42,62,63]), the discretized Lagrangian multipliers are updated in the $(k+1)$th iteration as follows:

$$\begin{cases} \left(\left(\Delta\gamma_{\mathrm{p}}^{(i)}\right)^{k+1} = \left(\Delta\gamma_{\mathrm{p}}^{(i)}\right)^{k} + \Delta\left(\Delta\gamma_{\mathrm{p}}^{(i)}\right)^{k+1}\right)_{(\mathrm{n}+1)(\mathfrak{t})} & i \in \mathcal{A}_{\mathrm{act}}; \\ \left(\left(\Delta\gamma_{\mathrm{d}}\right)^{k+1} = \left(\Delta\gamma_{\mathrm{d}}\right)^{k} + \Delta\left(\Delta\gamma_{\mathrm{d}}\right)^{k+1}\right)_{(\mathrm{n}+1)(\mathfrak{t}).} & \end{cases} \tag{40}$$

Once convergence is reached in the interior Newton-Raphson iteration, all relevant resultants are updated for the $(\mathrm{n}+1)$th global nonlinear iteration within the $\mathfrak{t}$ global time-incremental step. These updated variables include the stress $\mathbf{S}$, strain tensor $\mathbf{E}$, virgin energies $\Psi^{\mathrm{e}*}$ and $\Psi^{\mathrm{p}*}$, and internal state variables $\xi^{(i)}$ and η. Additionally, the inverse of the Jacobian matrixat the converged state, $(\mathrm{d}\phi/\mathrm{d}\boldsymbol{\Delta\gamma})^{-1}$, is essential for deriving the consistent tangent operators [33]. Applying the plastic Oldroyd-type material rate $\mathscr{L}_{\boldsymbol{\Delta}\mathbf{u}}^{\mathrm{p}}$ causes the second Piola–Kirchhoff stress $\hat{\mathbf{S}}$, the coupling force a^{m}, and the micromorphic force $\mathbf{b}^{\mathrm{m}}$ to vary with the global variables: the elastic Green–Lagrange strain $\mathbf{E}^{\mathrm{e}}(\mathbf{u})$ and micromorphic damage variable $\widetilde{\eta}$. This variation is derived from the constitutive relations in Section 2.4:

$$\begin{aligned} \mathscr{L}_{\boldsymbol{\Delta}\mathbf{u}}^{\mathrm{p/contra}}\left(\hat{\mathbf{S}}\right)_{\mathfrak{t}} &= \hat{\mathbb{C}}_{\mathfrak{t}}^{\mathrm{epd}} : \mathscr{L}_{\boldsymbol{\Delta}\mathbf{u}}^{\mathrm{p/co}}\left(\mathbf{E}^{\mathrm{e}}\right) + \hat{\mathbb{D}}_{\mathfrak{t}}^{\mathrm{S}\widetilde{\eta}}\Delta\widetilde{\eta}, \\ \Delta a_{\mathfrak{t}}^{\mathrm{m}} &= -\mathbb{P}_{\mathfrak{t}}\hat{\mathbb{A}}_{\mathfrak{t}}^{\eta\mathrm{E}} : \mathscr{L}_{\boldsymbol{\Delta}\mathbf{u}}^{\mathrm{p/co}}\left(\mathbf{E}^{\mathrm{e}}\right) + \mathbb{P}_{\mathfrak{t}}\left(1 - \hat{\mathbb{D}}_{\mathfrak{t}}^{\eta\widetilde{\eta}}\right)\Delta\widetilde{\eta}, \\ \mathbb{P}_{\mathfrak{t}} &= \frac{\partial a^{\mathrm{m}}}{\partial\widetilde{\eta}} = \exp\left[\widetilde{\eta}_{\mathfrak{t}} - \eta_{\mathfrak{t}}\right]\left(1 - \eta_{\mathfrak{t}} + \widetilde{\eta}_{\mathfrak{t}}\right)H^{\mathrm{m}}, \\ \Delta\mathbf{b}_{\mathfrak{t}}^{\mathrm{m}} &= A^{\mathrm{m}}\Delta(\nabla_{\boldsymbol{X}}\widetilde{\eta}). \end{aligned} \tag{41}$$

Alternatively, the variations in the stress $\hat{\mathbf{S}}$, forces a^{m} and $\mathbf{b}^{\mathrm{m}}$ can be expressed in terms of the internal state variables:

$$\begin{aligned} \left(\Delta\hat{\mathbf{S}}\right)_{\mathfrak{t}} &= 2\frac{\partial\hat{\mathbf{S}}}{\partial\mathbf{C}^{\mathrm{e}}} : \frac{1}{2}\Delta\mathbf{C}^{\mathrm{e}} + \frac{\partial\hat{\mathbf{S}}}{\partial\mathrm{D}}\frac{\partial\mathrm{D}}{\partial\Delta\gamma_{\mathrm{d}}}\Delta\left(\Delta\gamma_{\mathrm{d}}\right), \\ \Delta a_{\mathfrak{t}}^{\mathrm{m}} &= \frac{\partial a^{\mathrm{m}}}{\partial\eta}\frac{\partial\eta}{\partial\Delta\gamma_{\mathrm{d}}}\Delta\left(\Delta\gamma_{\mathrm{d}}\right) + \frac{\partial a^{\mathrm{m}}}{\partial\widetilde{\eta}}\Delta\widetilde{\eta}. \end{aligned} \tag{42}$$

A direct variation of the criteria is derived to satisfy the consistency condition for the coupled damage–plasticity problem. The time-discretized Lagrangian multipliers, $\Delta(\Delta\gamma_{\mathrm{p}}^{(i)})$ and $\Delta(\Delta\gamma_{\mathrm{d}})$, are replaced by $\mathscr{L}_{\boldsymbol{\Delta}\mathbf{u}}^{\mathrm{p/co}}(\mathbf{E}^{\mathrm{e}})$ and $\Delta\widetilde{\eta}$. Consequently, the four components of the consistent tangent operators are calculated and pulled back to the reference configuration. This concludes the standard finite element procedure for the $(\mathrm{n}+1)$th global nonlinear iteration within the global $\mathfrak{t}$ time increment.

Although this algorithm for updating the stress and consistent tangent operators is mathematically robust, it is numerically challenging due to the strong coupling between the strain-rate-independent single crystal plasticity and micromorphic continuum damage mechanisms. This conventional stress-update algorithm is also detailed in Appendix B. The Jacobian matrix $\mathrm{d}\phi/\mathrm{d}\boldsymbol{\Delta\gamma}$ in Eq. (39), evaluated at kth iteration, are given as follows:

$$
\begin{aligned}
\frac{\mathrm{d}\phi^{\mathrm{m}}}{\mathrm{d}\Delta\gamma_{\mathrm{d}}} &= \begin{cases} -\exp\left[-\mathrm{D}_{\mathrm{t}}\right]\left(\Psi^{\mathrm{e}*}+\alpha\Psi^{\mathrm{p}*}\right)_{\mathrm{t}} \\ +\exp\left[-\mathrm{\eta}_{\mathrm{t}}\right]\left(\Psi_0^{\mathrm{d}}+H^{\mathrm{d}}\eta_{\mathrm{t}}+H^{\mathrm{m}}\exp\left[\widetilde{\eta}_{\mathrm{t}}\right]\left(\eta_{\mathrm{t}}-\widetilde{\eta}_{\mathrm{t}}\right)\right) \\ -\exp\left[-\mathrm{\eta}_{\mathrm{t}}\right]\left(H^{\mathrm{d}}+H^{\mathrm{m}}\exp\left[\widetilde{\eta}_{\mathrm{t}}\right]\right); \end{cases} \\
\frac{\mathrm{d}\phi^{\mathrm{m}}}{\mathrm{d}\Delta\gamma_{\mathrm{p}}^{(i)}} &= -\phi^{\mathrm{p}(i)}-(1-\alpha)\left(\tau_{\mathrm{c}}^{*(i)}Q^{(i)}\right)_{\mathrm{t}}; \\
\frac{\mathrm{d}\phi^{\mathrm{p}(i)}}{\mathrm{d}\Delta\gamma_{\mathrm{d}}} &= -\exp\left[-\mathrm{D}_{\mathrm{t}}\right]\left(|\tau_{\mathrm{r}}^{*(i)}|_{\mathrm{t}}-\alpha\left(\tau_{\mathrm{c}}^{*(i)}Q^{(i)}\right)_{\mathrm{t}}\right); \\
\frac{\mathrm{d}\phi^{\mathrm{p}(i)}}{\mathrm{d}\Delta\gamma_{\mathrm{p}}^{(j)}} &= \begin{cases} -\operatorname{sign}\left(\tau_{\mathrm{r}}^{(i)}\right)_{\mathrm{t}}\operatorname{sign}\left(\tau_{\mathrm{r}}^{(j)}\right)_{\mathrm{t}}\Big(2\operatorname{sym}\left\{\mathbf{C}_{\mathrm{t}}^{\mathrm{e}}\mathbf{N}^{\mathrm{p}(j)}\right\}\hat{\mathbf{S}}_{\mathrm{t}} \\ +\mathbf{C}_{\mathrm{t}}^{\mathrm{e}}\hat{\mathbb{C}}^{\mathrm{e}} : \operatorname{sym}\left\{\mathbf{C}_{\mathrm{t}}^{\mathrm{e}}\mathbf{N}^{\mathrm{p}(j)}\right\}\Big) : \mathbf{N}^{\mathrm{p}(i)} \\ -\left(Q^{(i)}Q^{(j)}\dfrac{\partial\tau_{\mathrm{c}}^{(i)}}{\partial\xi^{(j)}}\right)_{\mathrm{t}}-\left(\tau_{\mathrm{c}}^{(i)}\dfrac{\partial Q^{(i)}}{\partial\Delta\gamma_{\mathrm{p}}^{(j)}}\right)_{\mathrm{t}}, \end{cases}
\end{aligned}
\tag{43}
$$

Direct observation of the Jacobian matrix reveals that the interior linearized algebraic system is symmetric. This feature allows for the use of a robust linear solver at the local level.

3.1.3. Sequential plasticity–damage algorithm

Given the challenges in coupling strain-rate-independent single crystal plasticity with micromorphic damage extension, the proposed sequential algorithm can be considered a special case of the general model. For this simplified algorithm, the condition ($\alpha = 1$) in Eq. (28) must hold, implying that the elastic and plastic contributions to the damage process are equal. This assumption is reasonable for ductile fracture analysis, especially for metals, where plastic strain is the primary driver of the damage process (see 3.1.3 Note (1)).

At the converged state of the Newton-Raphson iteration, Eq. (43) can be rewritten as:

$$
\begin{aligned}
\frac{\mathrm{d}\phi^{\mathrm{m}}}{\mathrm{d}\Delta\gamma_{\mathrm{d}}} &= -\exp\left[-\eta_{\mathrm{t}}\right]\left(H^{\mathrm{d}}+H^{\mathrm{m}}\exp\left[\widetilde{\eta}_{\mathrm{t}}\right]\right); \\
\frac{\mathrm{d}\phi^{\mathrm{m}}}{\mathrm{d}\Delta\gamma_{\mathrm{p}}^{(i)}} &= \frac{\mathrm{d}\phi^{\mathrm{p}(i)}}{\mathrm{d}\Delta\gamma_{\mathrm{d}}} = -\phi^{\mathrm{p}(i)} \approx 0; \\
\frac{\mathrm{d}\phi^{\mathrm{p}(i)}}{\mathrm{d}\Delta\gamma_{\mathrm{p}}^{(j)}} &= \exp\left[-\mathrm{D}_{\mathrm{t}}\right]\frac{\mathrm{d}\phi^{\mathrm{p}*(i)}}{\mathrm{d}\Delta\gamma_{\mathrm{p}}^{(j)}}.
\end{aligned}
\tag{44}
$$

Notably, the off-diagonal coupling terms $\frac{\mathrm{d}\phi^{\mathrm{m}}}{\mathrm{d}\Delta\gamma^{(i)}\mathrm{p}}$ and $\frac{\mathrm{d}\phi^{\mathrm{p}(i)}}{\mathrm{d}\Delta\gamma_{\mathrm{d}}}$ depend on the plastic yield function, $\phi^{\mathrm{p}(i)}$, which approaches zero upon convergence of the internal return-mapping algorithm. Furthermore, the Jacobian term ($\mathrm{d}\phi^{\mathrm{p}(i)}/\mathrm{d}\Delta\gamma_{\mathrm{p}}^{(j)}$) simplifies to a product of the degradation function, $\exp\left[-\mathrm{D}_{\mathrm{t}}\right]$, and the corresponding Jacobian component of the undamaged plasticity model. In this case, the plasticity calculation is naturally separated from the damage calculation. Consequently, the plastic KKT condition (Eq. (36)) is satisfied if either the material is fully damaged ($f(\mathrm{D}) \approx 0$) or the return-mapping for the pure single-crystal plasticity is complete ($\phi^{(i)}\mathrm{p} \leq 0\ \forall i$). The trial criteria are rewritten as:

$$
\phi_{\mathrm{t}}^{\mathrm{p}(i),\mathrm{trial}} = \exp\left[-\mathrm{D}_{t_{\mathrm{n}}}\right]\left(\left|\tau_{\mathrm{r}}^{*(i),\mathrm{trial}}\right|_{\mathrm{t}}-\left(\tau_{\mathrm{c}}^{*(i)}\right)_{t_{\mathrm{n}}}\right), \tag{45}
$$

$$
\phi_{\mathrm{t}}^{\mathrm{m},\mathrm{trial}} = \exp\left[-\mathrm{D}_{t_{\mathrm{n}}}\right]\left(\Psi_{\mathrm{t}}^{\mathrm{e}*}+\Psi_{\mathrm{t}}^{\mathrm{p}*}-\left(\beta_{t_{\mathrm{n}}}^{\mathrm{d}*}+\beta_{\mathrm{t}}^{\mathrm{m}*,\mathrm{trial}}\right)\right). \tag{46}
$$

Here, the virgin microscopic damage $\beta^{\mathrm{d}*}(\eta)$ and micromorphic $\beta^{\mathrm{m}*}\left(\eta-\widetilde{\eta}\right)$ are defined. The damage calculation thus becomes a simple post-processing step performed after the elasto-plastic deformation is calculated. As a result, the conventional stress-update algorithm from Section 3.1.2 simplifies significantly into a sequential scheme. For example, using the constitutive relations from Section 2.4, an explicit solution for the damage variable can be found:

$$
\begin{aligned}
\beta^{(\mathrm{d}+\mathrm{m})*} &= \Psi_0^{\mathrm{d}}+\left(H^{\mathrm{d}}+H^{\mathrm{m}}\exp\left[\widetilde{\eta}\right]\right)\eta-H^{\mathrm{m}}\exp\left[\widetilde{\eta}\right]\widetilde{\eta}, \\
\eta_{\mathrm{t}} \equiv \mathrm{D}_{\mathrm{t}} &= \frac{(\Psi^{\mathrm{e}*}+\Psi^{\mathrm{p}*})_{\mathrm{t}}-\Psi_0^{\mathrm{d}}+H^{\mathrm{m}}\exp\left[\widetilde{\eta}_{\mathrm{t}}\right]\widetilde{\eta}_{\mathrm{t}}}{H^{\mathrm{d}}+H^{\mathrm{m}}\exp\left[\widetilde{\eta}_{\mathrm{t}}\right]},
\end{aligned}
\tag{47}
$$

where the variables η and D are taken as the converged interior variables once the global nonlinear iteration is complete. In contrast, the conventional approach requires that the variables $\boldsymbol{\xi}_{\mathrm{t}}$ and η_{t} must be evolved simultaneously using the systems described in Eqs. (33), (34) and (40).

Note (1). The modeling assumption ($\alpha = 1$) corresponds to the right side of the framework shown in Fig. 1. In this case, the decoupling procedure combines the condition ($\alpha = 1$) with a expedient analytical expression for the damage evolution. Quantities in the fictitious undamaged configuration, denoted by $(\bullet)^*$, are scaled by the volume fraction $f(\mathrm{D})$. This allows the undamaged elasto-plastic

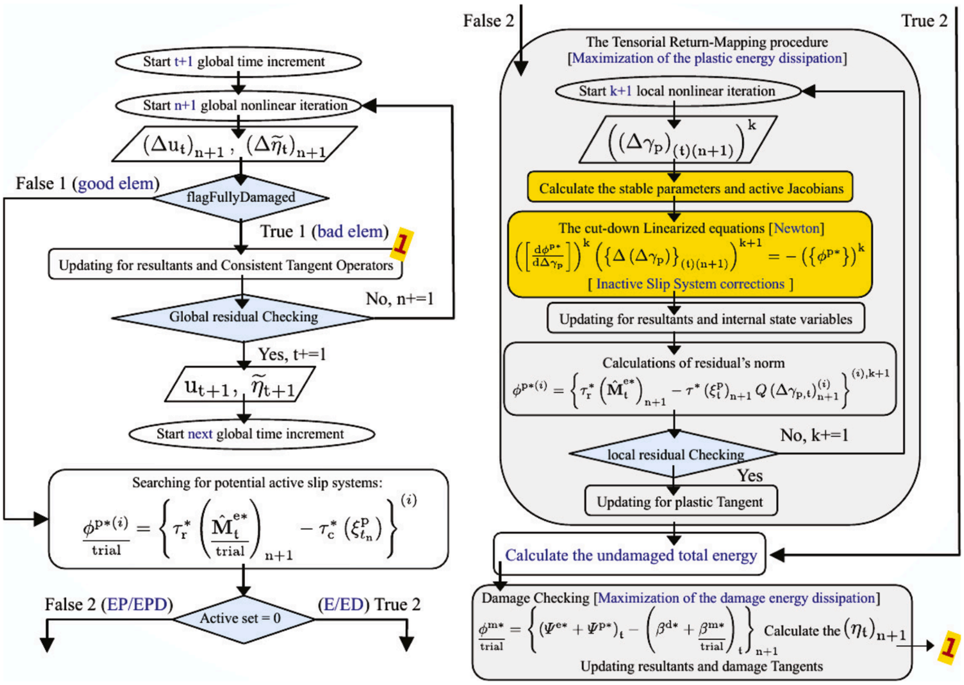

Fig. 2. Sequential algorithm under the standard finite element procedure.

response and the virgin micromorphic damage evolution to be treated separately, as shown conceptually by the boxes labeled $(\bullet)^*$. The micromorphic damage mechanism is a novel aspect of the proposed continuum damage model. The box marked $(\bullet)^*$ for the damage mechanism is consistent with using the damage characterization $\beta^{(d+m)*}$. For instance, according to Eqs. (23) and (24), the term Ψ^d describes the nucleation and growth of microscopic voids or cracks via the volume fraction term "$(1 - \exp[-\eta])$". In contrast, the term Ψ^m describes an additional growth mechanism induced by length scales, represented by the term "$(1 - \exp[\widetilde{\eta} - \eta])$". In the general case, the specific connection between the damage mechanisms is not constrained. The quasi-brittle fracture behavior is discussed in Appendix A. In this appendix, the implicit characteristic length l_c is shown to vary with three damage-growth mechanisms. The results demonstrate consistency when the term $(\widetilde{\eta} - \eta)$ approaches zero, at which point the formulation reduces to the PF damage model.

The sequential plasticity–damage algorithm is summarized in Fig. 2, algorithmically illustrating the right side of the proposed framework (Fig. 1). While improving global robustness is not the primary focus, the standard finite element procedure with $(n+1)$th nonlinear iteration during $(t+1)$ time increment is followed. The search for the potential active set for plasticity is performed using trial value $\phi^{p*(i)}$ from Eqs. (45) and (46). Here, "E", "P", and "D" signify the elastic, plastic, and damaged states, which depend on the active set $\mathcal{A}^s_{act}$ (where "s" denotes sequential). It is noteworthy that $\mathcal{A}^s_{act}$ does not need to account for the damaged state, unlike the set $\mathcal{A}^c_{act}$ ("c" for conventional) in the conventional algorithm (see Appendix B for a detailed discussion). After the potential active set is defined, the sequential procedure proceeds from the elasticity block to the plasticity block (if the active set is not empty) and finally to the damage block. This sequence, from $\phi^{p*(i)}$, Ψ^{total*} to ϕ^{m*}, is encapsulated within the framework shown in Fig. 1.

Other plasticity models, such as Drucker–Prager plasticity [64] or plasticity with a yield-point phenomenon [65], can be considered by replacing the plasticity block. Similarly, other damage processes, such as an exponential growth mechanism, can be modeled through the damage block, provided they follow the assumptions mentioned in Note 3.1.3. Essentially, the interior Jacobians in Eq. (39) and the consistent tangent operators in Eq. (41) can be significantly simplified without losing mathematical equivalence. This suggests that the strong coupling in the conventional algorithm is a likely source of numerical divergence; thus, this sequential approach implicitly enhances numerical robustness in polycrystalline ductile fracture analyses.

4. Numerical examples

To demonstrate the performance and robustness of the proposed constitutive model in polycrystalline ductile fracture analysis, this section presents several numerical applications. These applications are divided into two main categories:

1. Single crystal sheet problems: These applications investigate the mechanisms triggering strain localization. The geometric setup and boundary conditions are detailed in Fig. 3.
2. Polycrystalline material systems: Various applications within these systems are explored.

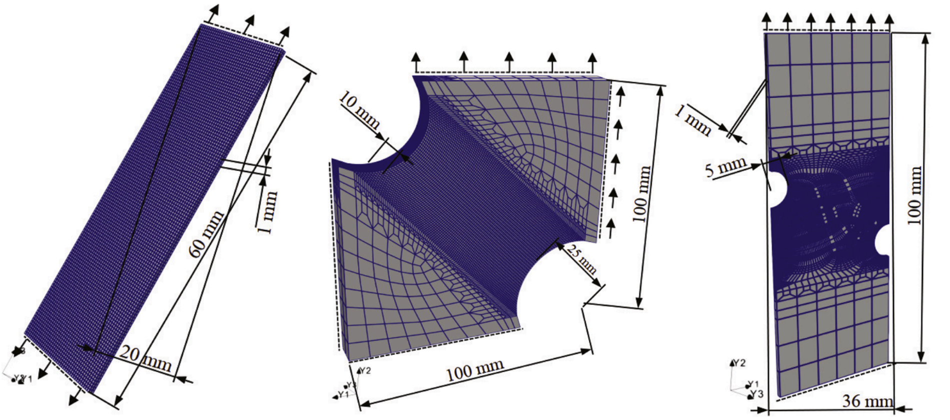

(a) Single crystal sheet (b) Double pre-notched unsymmetric specimens 1 (c) Double pre-notched unsymmetric specimens 2

Fig. 3. Schematic of the specimen geometries and boundary conditions used in the numerical examples.

The study first emphasizes the influence of imperfections on inducing localization. Subsequently, it discusses the microstructural features of polycrystals using a finite element model with idealized, periodically arranged equiaxial grains. The **F**-bar method [66,67] was used for strain-stabilization to avoid volumetric locking.

4.1. Application 1: strain localization of single crystal sheet

The problem of a single crystal sheet is based on an example in the single crystal plasticity section of de Souza Neto et al. [67]. The reference examples uses two different meshes: one with 2752 nodes and 1200 8-node hexahedral elements, and another with 15,432 nodes and 9600 elements. While that reference considered a double-slip system and purely elastoplastic behavior, the present study investigates a damageable material and single crystal plasticity with the slip systems of a FCC crystal. The material parameters are provided in Table 1. Following the referenced example, isotropic elasticity is assumed, which is considered reasonable for this application because the elastic (lattice) distortion is relatively small. From a numerical perspective, it is crucial to recognize that both geometrical and local material imperfections can induce strain localization. In the first strain localization problem, the specimen's [111] crystal orientation matches the loading direction (Y3), as shown in Fig. 4(a) and (b). In this case, a material imperfection is introduced at the specimen's central point by defining a locally weaker material response (i.e., a lower yield stress). After the peak-load point, geometrical softening of the finite strain is observed, as shown in Fig. 4(d). At this point, the plastic material imperfection induces strong specimen necking, which is concentrated around the imperfection and is orthogonal to the loading (Y3) direction. Damage (solid material degradation) initiates at this imperfection and propagates within the elastoplastic zone, which enhances the plastic strain localization. Conversely, this localization accelerates damage growth (i.e., voids and cracks), as seen in the comparison between Fig. 4(d) and the referenced example from de Souza Neto et al. [67]. Furthermore, mesh independence of the first strain-localization problem (Fig. 4(a) and (b)) was investigated using several refined meshes. The results demonstrate good regularization of the damage process, as discussed by Tan and Watanabe [33] and Brepols et al. [32].

In addition, crystallographic misorientation is another essential trigger for strain localization. A numerical example without initial imperfections is performed, with the results shown in Fig. 4(c). The single crystal sheet has an initial [112] crystallographic orientation, which results in misorientation at the midpoint between the [100] and [111] directions relative to the loading direction (Y3). The material parameters were chosen with a higher critical resolved shear stress of $\tau_0^{(i)} = 60$ MPa, as shown in Fig. 4(d). In this case, damage initiation does not occur at the central point but at locations with large plastic strain localization caused by rotation. With further material deformation, plastic strain accumulates unsymmetrically along the central section. Consequently, the damage profile changes to a shear band that is misoriented relative to the loading direction (Y3), as shown in Fig. 4(c), leading to rapid strength degradation.

Furthermore, the comparative result for the normalized residual during the global nonlinear Newton iteration are shown in Fig. 4(d) and Table 2. After scaling the variables, both the elastoplastic (Stage 1) and post-peak-load (Stage 2) states exhibit a quadratic convergence rate. However, as material nonlinearity and damage localization increase, Stage 2 requires more iterations than Stage 1. This observation is consistent with the convergence analysis in Brepols et al. [32]. Additionally, the same trends were observed in other numerical examples within this study.

The notched single crystal sheet problems are based on the work of Tan and Watanabe [33] and Felder et al. [68]. One model uses a mesh with 101,840 nodes and 90,314 8-node hexahedral elements, while the other uses 19,100 nodes and 13,866 elements. For both models, a 1 % thickness reduction at the notch, an initial [111] crystal orientation, and a loading direction along the Y2-axis

Table 1
Material constants used in the numerical examples. The symbol x indicates a parameter that was varied.

Material constants	Symbol	Unit	Section 4.1	Section 4.2
Elasticity (Eq. (17))				
Elastic modulus	$\hat{\mathbb{C}}^{e}_{1111}$	(GPa)	(E)73.67	170.0
(crystal configuration)	$\hat{\mathbb{C}}^{e}_{1122}$	(GPa)	(ν)0.31	120.0
	$\hat{\mathbb{C}}^{e}_{1212}$	(GPa)	(-)	75.0
Plasticity (Eqs. (18) and (20))				
Lattice structure			FCC	FCC
Initial critical resolved shear stress	$\tau_0^{(1)}$	(MPa)	60.0/54.0	100.0
Linear hardening modulus	$H^{p(1)}$	(MPa)	0.0	10.0
Latent hardening matrix	$\Omega_{ij}^{(1)} (i \neq j)$	(-)	1.0	1.1
Relative saturated shear stress	$\delta\tau_s^{(1)}$	(MPa)	48.0/54.0	100.0
Reference material strength	$h^{p(1)}$	(MPa)	520.0	100.0
Rate dependent sensitivity	r_a	(-)	2.0	2.0
Rate dependent modulus	r_b	(-)	0.5	0.5
Damage (Eq. (23))				
Damage energy threshold	Ψ_0^{d}	(mJ/mm^3)	100.0	50.0
Hardening modulus	H^{d}	(mJ/mm^3)	50.0	25.0
Micromorphic damage (Eq. (24))				
Micromorphic modulus	A^{m}	(mJ/mm)	100.0	x
Coupling parameter	H^{m}	(mJ/mm^3)	10^4	10^4

Table 2
Global convergence rates at the two stages in Fig. 4.

Iteration	Residual (Stage 1)		Residual (Stage 2)	
	[111] (Fig. 4(a))	[112] (Fig. 4(c))	[111] (Fig. 4(a))	[112] (Fig. 4(c))
0	1.000000E + 00	1.000000E + 00	1.000000E + 00	1.000000E + 00
1	7.937306E - 02	7.355792E - 02	1.140483E - 02	2.008108E - 02
2	1.434474E - 06	3.415050E - 04	4.267915E - 04	1.695703E - 02
3	8.448759E - 11	7.685361E - 06	1.359574E - 04	3.284871E - 04
4	–	1.961849E - 07	6.919910E - 05	6.275279E - 05
5	–	8.954857E - 11	1.014185E - 06	1.106686E - 05
6	–	–	1.600235E - 07	4.588292E - 06
7	–	–	7.516613E - 11	1.273661E - 06
8	–	–	–	1.307343E - 11

were considered. The material parameters, including the damage energy threshold ($\Psi_0^{d} = 50$) and hardening modulus ($H^{d} = 30$), are taken from Table 1.

The damage initiation shown in Fig. 5 is unsymmetric in the single crystal case (Fig. 5(b)), in contrast to the symmetric behavior observed in isotropic ductile fracture analysis (Fig. 5(a)). This distinction is significant for subsequent damage propagation and the formation of unsymmetric crack surfaces between the two pre-notches. The explanation for this unsymmetric damage initiation can be found in the context of the second strain-localization mode due to misorientation, as depicted in Fig. 4(c). These notched examples demonstrate an extremely ductile material response, characterized by a material softening phase where the unsymmetric crack paths have not yet connected, and a necking phase where strain localizes around the area of damage coalescence (as shown in the specimen deformation of Fig. 5). This underscores the necessity of three-dimensional ductile fracture analysis with crystal plasticity to accurately analyze damage initiation and propagation.

The investigation concludes that the two factors for strain localization, while both considered material imperfections, represent distinct trigger mechanisms. These mechanisms lead to different magnitudes of strength degradation and exhibit either symmetric or unsymmetric strain localization, while maintaining a strong interaction in polycrystalline material systems.

4.2. *Application 2: polycrystalline ductile fracture analysis*

This section demonstrates the application of the proposed approach to periodic polycrystalline aggregates to emphasize the improvement in computational robustness. The FE model (Fig. 6) consists of 128 grains with an idealized truncated octahedron geometry. The model is composed of 40,113 nodes and 36,864 8-node hexahedral elements. The material constants are listed in Table 1. Notably, the strain-rate-dependence parameters are set to produce a response that is nearly identical to that of a strain-rate-independent model. FCC slip systems are employed for the single crystal plasticity, and the crystallographic orientations of the grains are assigned randomly. The $\{111\}$ pole figure is shown in Fig. 7. FE analyses were performed by imposing a macroscopic uniaxial tensile strain mode on the periodic microstructure in the Y1, Y2, and Y3 directions.

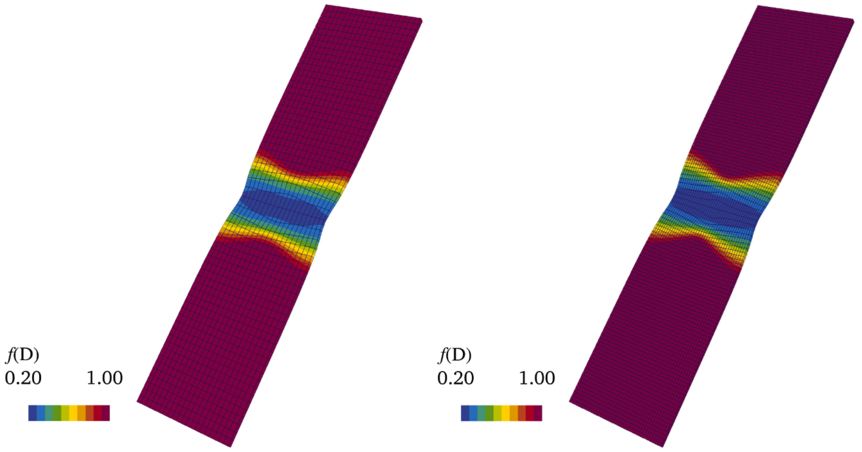

(a) [111] with imperfection (b) [111] with imperfection (finner mesh)

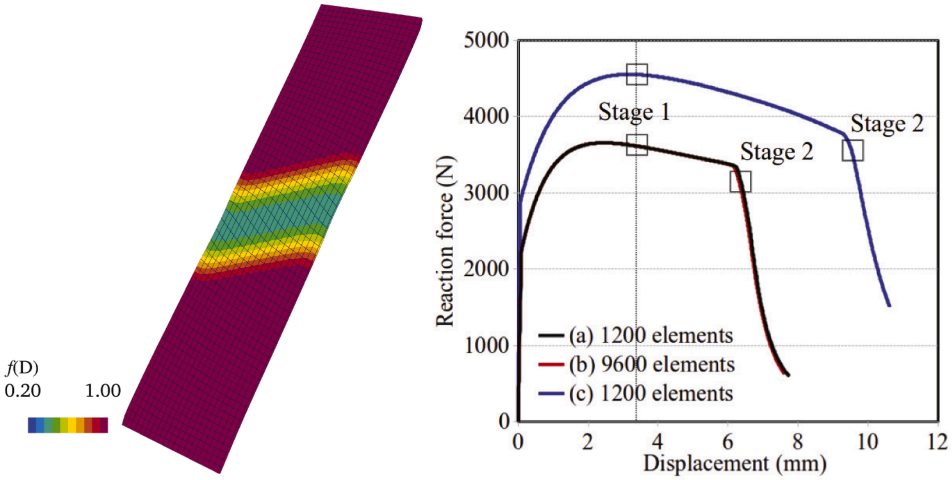

(c) [112] without imperfection (d) Reaction–force displacement curve

Fig. 4. Ductile fracture results for the single crystal sheet.

The von Mises stress and plastic strain distributions on the left side of Fig. 7 represent the state before damage initiation at a macroscopic axial strain 5 %. Damage evolves locally due to this heterogeneity. Fig. 7 presents the distributions of damage at macroscopic axial strain 14.4 % and 16.7 %. The damage regions connect and penetrate the periodic material microstructure, resulting in a degradation in macroscopic stiffness. In this case, almost identical macroscopic elastoplastic material responses were obtained under the three loading directions (Y1, Y2, and Y3), as quantitatively verified by the macroscopic stress–strain curves in Fig. 7.

In addition, another fiber crystallographic feature, characterized in the second $\{111\}$ pole figure of Fig. 7, was investigated. This fiber feature is verified by the distinctive strain-hardening observed between the (Y1, Y3) and Y2 loading directions. Under further deformation, damage initiation, primarily driven by plastic strain in ductile fracture analysis, is triggered on the surface, as seen in the comparison of (Y1-1), (Y2-1), and (Y3-1) in Fig. 7. The distribution among the three loading directions depends on the localized elastoplastic deformation and exhibits multi-point damage occurance. For instance, the main initiation occurs at long-spacing grain boundaries in (Y3-1) and at quadruple/triple junctions in (Y1-1) and (Y2-1). In the (Y2-1) case, two damage concentrations accumulate specifically at triple junctions.

From the simulation results, damage evolution follows two mechanisms: transgranular and intergranular propagation modes. Regarding further propagation, the results in (Y1-2), (Y2-2), and (Y3-2) indicate that the main mode presented in (Y3-2) is transgranular. This is explained by the primary contribution of microscopic shear bands, which link grain boundary damage initiations along paths within the grain, leading to damage coalescence (microscopic voids and cracks). While there are few shear bands within (Y2-2), localized damage growth rapidly degrades the surrounding grain area through a short-spacing intergranular feature. Although the damage in (Y1-1) initiated at grain boundaries and junction areas, transgranular propagation dominates in the (Y1-2)

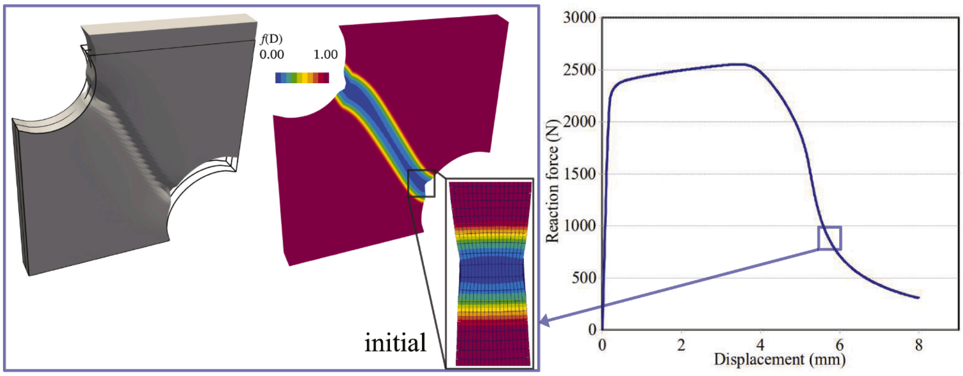

(a) Isotropic plasticity in Tan and Watanabe [33]

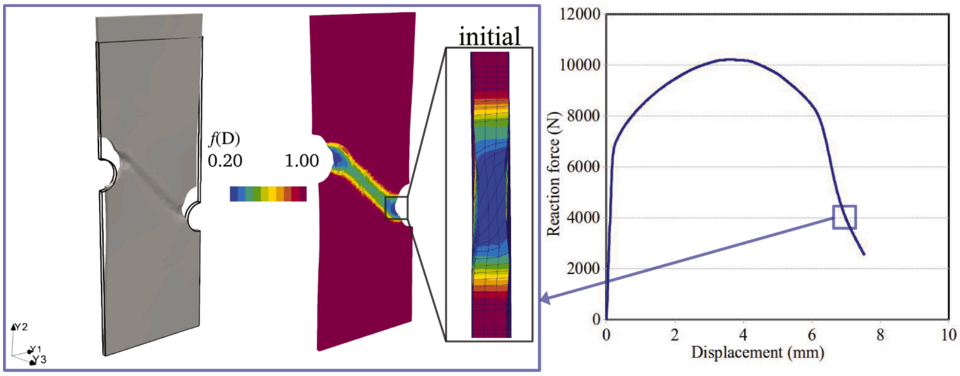

(b) Single crystal plasticity [111]

Fig. 5. Damage evolution in the double pre-notched specimen under loading in the Y2 direction.

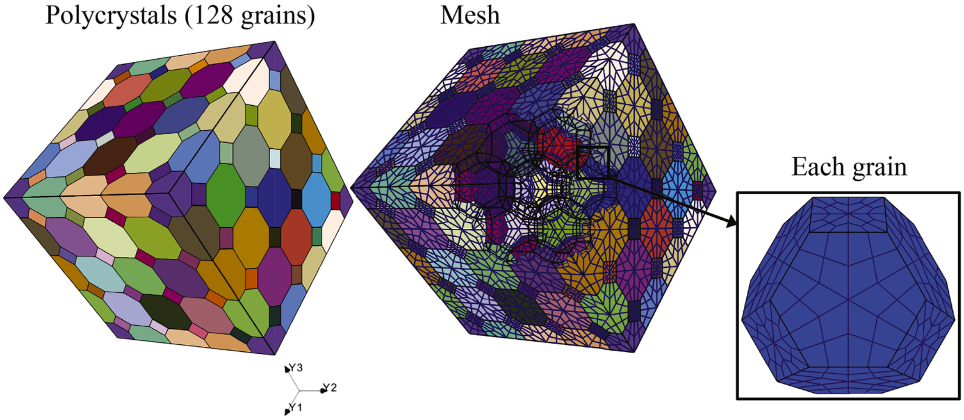

Fig. 6. Finite element model of a polycrystalline microstructure consisting of 128 grains with an idealized truncated octahedron geometry.

result, which contains numerous damage-induced shear bands. These results prove that the earliest damage initiation affects subsequent propagation modes, while the main factor determining ductile properties relates to the multi-point damage burst mechanism and the formation of microscopic damage-induced shear bands.

During further damage linkage and coalescence, microscopic damage shear bands coalesce and propagate unsymmetrically into the specimen interior, as shown in (Y1-3), (Y2-3), and (Y3-3). The quantitative stress–strain curves for Y1, Y2, and Y3 (with both random and fiber features) in Fig. 7 demonstrate that materials with identical macroscopic elastoplastic responses can exhibit distinct ductile properties. Specifically, when comparing the Y1 (black solid line) and Y2 (blue solid line) loading directions in the random

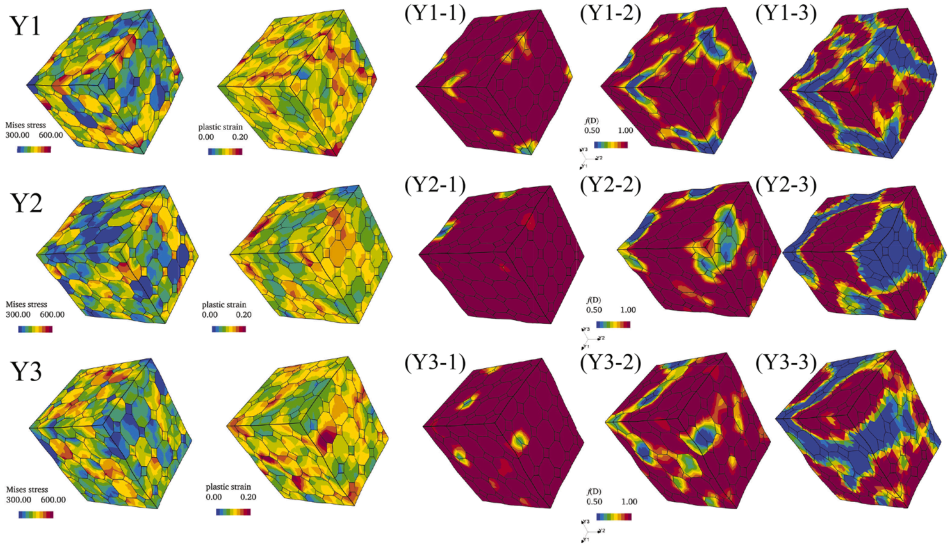

(a) von Mises stress(Y-1); Equivalent plastic strain(Y-1); Damage processes at macroxcopic strain, 5%, 14.4% and 16.7% (random orientations)

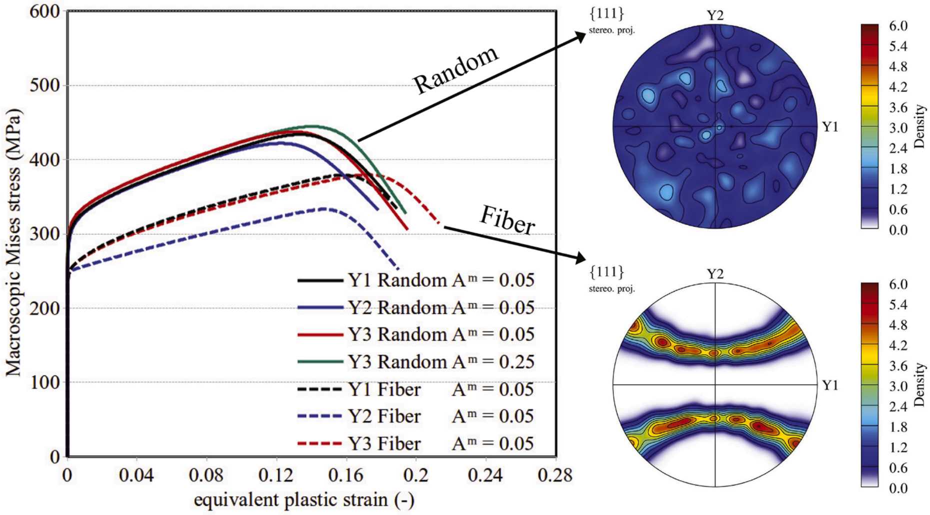

(b) Stress–strain curve (orientations and scale–lengths); {111} pole figures

Fig. 7. Ductile fracture results for the polycrystalline material system.

case, and the Y1 (black dashed line) and Y3 (red dashed line) loading directions in the fiber case, the reasons for the differences can be explained as follows:

1. A larger number of transgranular propagation modes along the shear bands results in a more ductile response.
2. A greater number of damage initiations at long-spacing grain boundaries increases the probability of shear band formation within the grain.

The micromorphic features of the model allow for the characterization of an intrinsic length scale. This is demonstrated by the comparison in Fig. 7 for the random microstructure along the Y3 direction, which was controlled by the material parameter A^{m} (selected as 0.05 or 0.25 mJ/mm for comparison). This length scale represents the width of the microscopic damage-induced shear bands within the representative volume element. This will be investigated in future studies on microstructural feature sensitivity. The mechanisms for damage initiation, propagation modes, and shear band formation are central to the analysis presented in this study, demonstrating the robustness of the proposed model for polycrystal ductile fracture analysis.

5. Conclusions

This study addressed the challenges associated with the implicit coupling between strain-rate-independent single crystal plasticity and micromorphic damage mechanisms. Specifically, a robust stress-update algorithm was proposed to overcome computational challenges in solving global equations and managing increased material instability, even in complex systems like polycrystalline ductile fracture analysis. This algorithm relies on a special condition ($\alpha = 1$) and is inspired by analytical solutions from the micromorphic framework, featuring a sequential algorithmic design. A comparison verified that the conventional and sequential algorithms maintain mathematical equivalence. Additionally, two ductile crystal examples were presented. The first demonstrated the distinctive trigger mechanisms of damage-induced strain localization, corresponding to different fracture modes. The second, when applied to polycrystalline systems, successfully characterized the damage mechanism, from damage initiation (Y-1) and the formation of microscopic shear bands (Y-2) to damage coalescence leading to strain localization (Y-3). The proposed model can analyze the effect of microstructural features, such as realistic material anisotropy and length scales associated with material ductility. These capabilities are attributed to the proposed modeling framework for micromorphic ductile materials and the natural separation of "plasticity" and "damage" mechanisms. This approach implicitly mitigates numerical challenges in obtaining stable solutions in polycrystalline ductile fracture analysis.

This study primarily focuses on the verification and algorithmic aspects of the damageable material model developed within a micromorphic framework. It provides a robust foundation for future polycrystalline applications, such as ductile fracture analysis in image-based polycrystalline models and coupling with other physical systems, including thermal creep and hydrogen embrittlement in polycrystalline materials.

CRediT authorship contribution statement

Tianwen Tan: Writing – review & editing, Writing – original draft, Visualization, Methodology, Investigation, Formal analysis, Data curation, Conceptualization; **Ikumu Watanabe:** Writing – review & editing, Writing – original draft, Supervision, Software, Resources, Project administration, Methodology, Investigation, Funding acquisition, Conceptualization.

Data availability

Data will be made available on request.

Declaration of competing interest

The authors declare that they have no known competing financial interests or personal relationships that could have appeared to influence the work reported in this paper.

Acknowledgments

This work was partly supported by the Japan Science and Technology Agency (JST) CREST grant numeber JPMJCR1995, Japan. We would also like to thank Editage for their English language editing services.

Appendix A. Similarity with the phase–field model and micromorphic damage mechanism

The standard formulation of a Phase-Field (PF) damage model for brittle fracture, referenced from Miehe et al. [58] and Wu [69], is presented below and solved globally:

$$\frac{1}{\mathrm{L}}\dot{\mathrm{D}} = 2(1-\mathrm{D})\left(\Psi^{\mathrm{e}*+}\right) - \frac{\mathrm{G_c}}{\mathrm{c}_0 l}\mathrm{D} + \frac{\mathrm{G_c} l}{\mathrm{c}_0}\nabla^2_{\boldsymbol{X}}\mathrm{D} \qquad \forall \boldsymbol{X} \in \Omega_0, \tag{A.1}$$

where L is the viscosity parameter, $\mathrm{G_c}$ is the critical fracture surface energy, c_0 is a scaling parameter, and l is a characteristic length that regularizes the sharp crack. The micromorphic damageable material is formulated to exhibit the same PF damageable material behavior:

$$\begin{aligned} &\phi^{\mathrm{m}} = 2(1-\mathrm{D})\left(\Psi^{\mathrm{e}*+}\right) - \Psi^{\mathrm{d}}_0 - H^{\mathrm{d}}\eta - H^{\mathrm{m}}\left(\eta - \widetilde{\eta}\right); \\ &H^{\mathrm{m}}\left(\eta - \widetilde{\eta}\right) + A^{\mathrm{m}}\nabla^2_{\boldsymbol{X}}\widetilde{\eta} = 0 \qquad \forall \boldsymbol{X} \in \Omega_0. \end{aligned} \tag{A.2}$$

In this brittle material model, the function "$(1-\mathrm{D})^2$" serves as the solid degradation function $f(\mathrm{D})$. The damage variable η is naturally bounded, with $\eta \in [0,1]$, for the selected Helmholtz free energy and the evolutions of the local state-dependent variables:

$$\begin{aligned} &\Psi^{\mathrm{d}} := \Psi^{\mathrm{d}}_0\eta + \frac{1}{2}H^{\mathrm{d}}\eta^2; \quad \beta^{\mathrm{d}} = \Psi^{\mathrm{d}}_0 + H^{\mathrm{d}}\eta; \\ &\Psi^{\mathrm{m}} := \frac{1}{2}H^{\mathrm{m}}\left(\eta - \widetilde{\eta}\right)^2 + \frac{1}{2}A^{\mathrm{m}}|\nabla_{\boldsymbol{X}}\widetilde{\eta}|^2; \quad \beta^{\mathrm{m}} = H^{\mathrm{m}}\left(\eta - \widetilde{\eta}\right); \\ &\dot{\mathrm{D}} = \dot{\eta}. \end{aligned} \tag{A.3}$$

The constrained micromorphic model is equivalent to the PF damage model under three conditions: (1) ($\Psi_0^{\mathrm{d}} \approx 0$), (2) ($H^{\mathrm{m}} \approx +\infty$), and (3) an identical evolution of D and η. This equivalence arises from a penalization that constrains the global micromorphic balance equation.

The time-discretized Lagrangian for the reduced dissipation of this brittle material system can be defined to satisfy the Karush–Kuhn–Tucker conditions. At the global $(\mathrm{n}+1)$th iteration of the (t) subtime-increment, the defined damage potential ϕ^{m} from Eq. (7) in the trial state is as follows:

$$\left(\Delta\gamma_{\mathrm{d}}\right)_{\mathrm{t}} \geqslant 0, \quad \phi^{\mathrm{m}} \leqslant 0, \quad \left(\Delta\gamma_{\mathrm{d}}\right)_{\mathrm{t}}\phi^{\mathrm{m}} = 0; \tag{A.4}$$

$$\phi_{\mathrm{t}}^{\mathrm{m,trial}} = 2\left(1 - \mathrm{D}_{t_{\mathrm{n}}}\right)\left(\Psi_{\mathrm{t}}^{\mathrm{e*+,trial}}\right) - \beta_{t_{\mathrm{n}}}^{\mathrm{d}} - H^{\mathrm{m}}\left(\eta_{t_{\mathrm{n}}} - \tilde{\eta}_{\mathrm{t}}^{\mathrm{trial}}\right). \tag{A.5}$$

The evolution equations for the two internal state variables, derived using a scalar Euler backward time-integration scheme, are:

$$\mathrm{D}_{\mathrm{t}} \equiv \eta_{\mathrm{t}} = \mathrm{D}_{t_{\mathrm{n}}} + \left(\Delta\gamma_{\mathrm{d}}\right)_{\mathrm{t}}, \tag{A.6}$$

Due to the convenient expression in Eqs. (A.4) and (A.5), the variables D and η can be obtained analytically:

$$\mathrm{D}_{\mathrm{t}} \equiv \eta_{\mathrm{t}} = \frac{\frac{2\Psi_{\mathrm{t}}^{\mathrm{e*+}} - \Psi_0^{\mathrm{d}}}{H^{\mathrm{m}}} + \tilde{\eta}_{\mathrm{t}}^{\mathrm{trial}}}{\frac{2\Psi_{\mathrm{t}}^{\mathrm{e*+}} + H^{\mathrm{d}}}{H^{\mathrm{m}}} + 1}. \tag{A.7}$$

This allows for a stress-update procedure without an interior Newton procedure during the global iteration $(\mathrm{n}+1)$ of the time increment (t).

Table A.1
Material constants (1) in comparison between Phase-Field model and micromorphic damage mechanism.

Damage Model	Young's modulus E [GPa]	Poisson's ratio ν [-]	Damage parameters
Phase-Field	210.0	0.3	$\mathrm{G_c}$ [mJ/mm^2] $l[mm]$ 2.7 0.02
Micromorphic	210.0	0.3	Ψ_0^{d}[mJ/mm^3] H^{d} [mJ/mm^3] $\approx$ 0 135 H^{m} [mJ/mm^3] A^{m} [mJ/mm] 10^4 0.054

Table A.2
Material constants (2) in comparison between Phase-Field model and micromorphic damage mechanism.

	Young's modulus E [GPa]	Poisson's ratio ν [-]	Damage parameters
Micromorphic	210.0	0.3	Ψ_0^{d} [mJ/mm^3] H^{d} [mJ/mm^3] $\approx$ 0 50 H^{m}[mJ/mm^3] A^{m}[mJ/mm] 10^4 0.01

The consistent (algorithmic) tangent matrix (CTM) is used to construct the global Jacobian matrix $(\mathbb{K})_{(\mathrm{n}+1)(\mathrm{t}_{\mathrm{n}+1})}$. First, the general case without constraints is derived:

$$\left(\begin{bmatrix} (1-\mathrm{D})^2\mathbb{C}^{\mathrm{e}} - \frac{4(1-\mathrm{D})^2\mathbf{S}^*\otimes\mathbf{S}^*}{2\Psi^{\mathrm{e*}}+H^{\mathrm{d}}+H^{\mathrm{m}}} & -\frac{H^{\mathrm{m}}}{2\Psi^{\mathrm{e*}}+H^{\mathrm{d}}+H^{\mathrm{m}}}2(1-\mathrm{D})\mathbf{S}^* & 0 \\ -\frac{H^{\mathrm{m}}}{2\Psi^{\mathrm{e*}}+H^{\mathrm{d}}+H^{\mathrm{m}}}2(1-\mathrm{D})\mathbf{S}^* & \frac{H^{\mathrm{m}}}{2\Psi^{\mathrm{e*}}+H^{\mathrm{d}}+H^{\mathrm{m}}}\left(2\Psi^{\mathrm{e*}}+H^{\mathrm{d}}\right) & 0 \\ 0 & 0 & A^{\mathrm{m}} \end{bmatrix}\right)_{(\mathrm{n}+1)(\mathrm{t}).} \tag{A.8}$$

The reduced version with constraints is then obtained:

$$\left(\begin{bmatrix} (1-\mathrm{D})^2\mathbb{C}^{\mathrm{e}} & -2(1-\mathrm{D})\mathbf{S}^* & 0 \\ -2(1-\mathrm{D})\mathbf{S}^* & 2\Psi^{\mathrm{e*}}+H^{\mathrm{d}} & 0 \\ 0 & 0 & A^{\mathrm{m}} \end{bmatrix}\right)_{(\mathrm{n}+1)(\mathrm{t})}; \qquad \mathrm{D}_{\mathrm{t}} \equiv \eta_{\mathrm{t}} = \tilde{\eta}_{\mathrm{t}}. \tag{A.9}$$

The PF brittle damage model corresponding to Eq. (A.1) is derived below:

$$\left(\begin{bmatrix} (1-\mathrm{D})^2\mathbb{C}^{\mathrm{e}} & -2(1-\mathrm{D})\mathbf{S}^* & 0 \\ -2(1-\mathrm{D})\mathbf{S}^* & 2\Psi^{\mathrm{e*}}+\frac{\mathrm{G_c}}{\mathrm{c}_0 l} & 0 \\ 0 & 0 & \frac{\mathrm{G_c} l}{\mathrm{c}_0} \end{bmatrix}\right)_{(\mathrm{n}+1)(\mathrm{t}).} \tag{A.10}$$

Material constitutive equivalence is achieved through suitable selections of material parameters, such as the damage hardening parameter ($H^{\mathrm{d}} = \mathrm{G_c}/\mathrm{c}_0 l$) and micromorphic parameter ($A^{\mathrm{m}} = \mathrm{G_c} l/\mathrm{c}_0$). Crucially, the PF damage model is a special case of the micromorphic

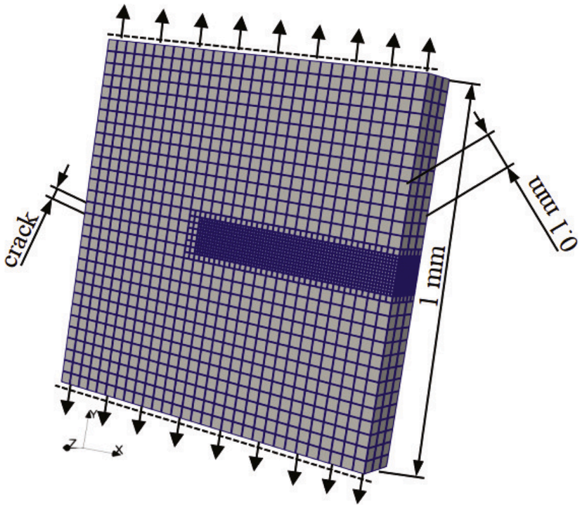

Fig. A.1. Schematic boundary conditions of the SENT test.

model under these assumptions. In addition, the semi-implicit ("staggered" or "alternative minimized") method proposed by Miehe et al. [57,58] was designed to modify the global time incremental step for model comparison.

The 3D single-edge notched tensile (SENT) test, a common benchmark in PF damage simulations, was employed. The material parameters for both models are listed in Table A. The analyzed domain was a unit plate with a 10 % thickness reduction at the notch. As shown in Fig. A.1, the model consists of 17,432 nodes and 13,368 8-node hexahedral elements with adaptive non-conforming mesh refinement. The plate was subjected to uniaxial tension at a rate of 2×10^{-5} mm/s to ensure consistency with the material parameters. Furthermore, a compressive Neo-Hookean hyperelasticity was employed with Young's modulus E and Poisson's ratio ν. The similarity between the models is presented in Fig. A.2, where a comparable profile of the damage variable D in the PF model and the micromorphic damage variable $\widetilde{\eta}$ in the micromorphic model was obtained, coinciding with the relationship defined in Eq. (A.9). In Fig. A.2(d), different values for the coupling parameter H^{m} are used. Smaller values of H^{m} result in a more quasi-brittle fracture response, indicating that $H^{\mathrm{m}}(\eta - \widetilde{\eta})$ acts as an additional local damage growth term. In this scenario, the damage zone evolves more rapidly after its initiation, and the model equivalence between the PF and micromorphic damage models becomes inconsistent.

On the other hand, it is essential to verify the proposed micromorphic damage energy Ψ^{m}. The constitutive material is modeled to describe quasi-brittle fracture, combining the exponential solid degradation function $f(\mathrm{D})$ with the linear damage mechanism based on the characterization of voids and cracks, Ψ^{d}, from Eq. (23). The local damage potential ϕ^{m} and the global micromorphic equilibrium were derived:

$$\begin{aligned} &\phi^{\mathrm{m}} = \exp[-\mathrm{D}]\left(\Psi^{\mathrm{e*+}}\right) - \underset{\text{locally (conventional)}}{\exp[-\eta]\left(\Psi_0^{\mathrm{d}} + H^{\mathrm{d}}\eta\right)} - H^{\mathrm{m}}\left(\eta - \widetilde{\eta}\right), \\ &\underset{\text{globally (conventional)}}{H^{\mathrm{m}}\left(\eta - \widetilde{\eta}\right) + A^{\mathrm{m}}\nabla^2_{\boldsymbol{X}}\widetilde{\eta} = 0} \qquad \forall \boldsymbol{X} \in \Omega_0, \end{aligned} \tag{A.11}$$

$$\begin{aligned} &\phi^{\mathrm{m}} = \exp[-\mathrm{D}]\left(\Psi^{\mathrm{e*+}}\right) - \underset{\text{locally (linear case)}}{\exp[-\eta]\left(\Psi_0^{\mathrm{d}} + H^{\mathrm{d}}\eta\right)} - H^{\mathrm{m}}\exp\left[\widetilde{\eta} - \eta\right]\left(\eta - \widetilde{\eta}\right), \\ &\underset{\text{globally (linear case)}}{H^{\mathrm{m}}\exp\left[\widetilde{\eta} - \eta\right]\left(\eta - \widetilde{\eta}\right) + A^{\mathrm{m}}\nabla^2_{\boldsymbol{X}}\widetilde{\eta} = 0} \qquad \forall \boldsymbol{X} \in \Omega_0. \end{aligned} \tag{A.12}$$

The difference between coupling terms becomes negligible as the term "$(\eta - \widetilde{\eta})$" approaches zero. However, this choice of formulation leads to a completely distinctive damageable material model, especially with larger coupling. Additionally, it can be modeled as an exponential damage growth mechanism:

$$\begin{aligned} \Psi^{\mathrm{m}} :=\; & H^{\mathrm{m}}\left(1 - \exp\left[\widetilde{\eta} - \eta\right] - \frac{1}{q^{\mathrm{d}} + 1}\left(1 - \exp\left[\left(q^{\mathrm{d}} + 1\right)\left(\widetilde{\eta} - \eta\right)\right]\right)\right) \\ & + \frac{1}{2}\nabla_{\boldsymbol{X}}\widetilde{\eta} \cdot \boldsymbol{A} \cdot \nabla_{\boldsymbol{X}}\widetilde{\eta}. \end{aligned} \tag{A.13}$$

The local damage potential ϕ^{m} and its equilibrium were derived:

$$\begin{aligned} &\phi^{\mathrm{m}} = \exp[-\mathrm{D}]\left(\Psi^{\mathrm{e*+}}\right) - \underset{\text{locally (exponential case)}}{\exp[-\eta]\left(\Psi_0^{\mathrm{d}} + H^{\mathrm{d}}\eta\right) - H^{\mathrm{m}}\exp\left[\widetilde{\eta} - \eta\right]}\left(1 - \exp\left[q^{\mathrm{d}}\left(\widetilde{\eta} - \eta\right)\right]\right), \\ &\underset{\text{globally (exponential case)}}{H^{\mathrm{m}}\exp\left[\widetilde{\eta} - \eta\right]\left(1 - \exp\left[q^{\mathrm{d}}\left(\widetilde{\eta} - \eta\right)\right]\right) + A^{\mathrm{m}}\nabla^2_{\boldsymbol{X}}\widetilde{\eta} = 0} \qquad \forall \boldsymbol{X} \in \Omega_0. \end{aligned} \tag{A.14}$$

From the perspective of obtaining an analytical solution, the damage D and microscopic damage variables η can be directly obtained only in the linear case (Eq. (A.12)), similar to the calculation in Eq. (47), except for the plastic contribution. Conversely, for the

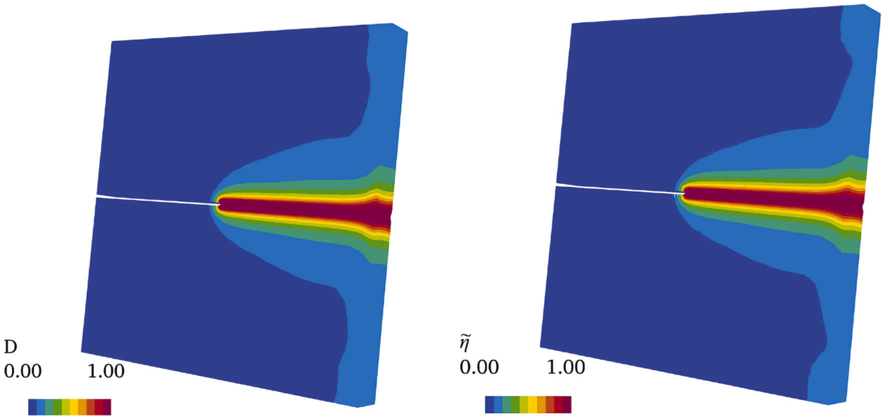

(a) (a) Phase-Field model (b) (b) Micromorphic model ($H^{\mathrm{m}} = 10^4$)

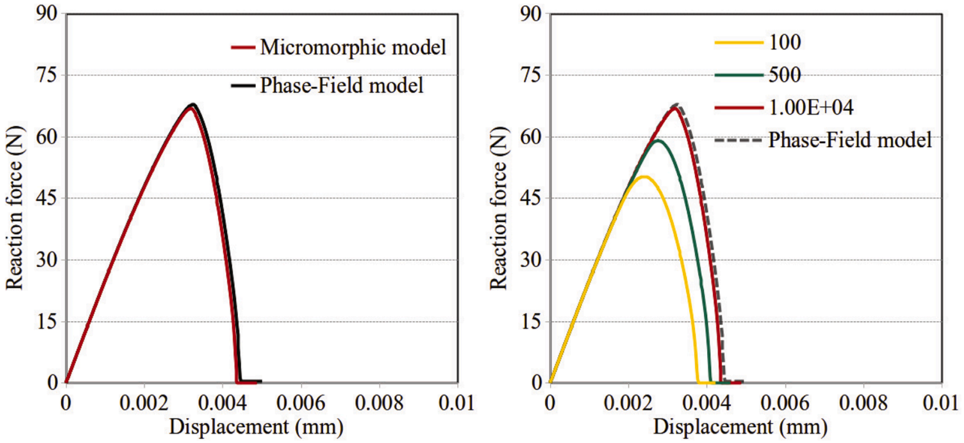

(c) (c) Model comparison ($H^{\mathrm{m}} = 10^4$) (d) (d) Sensitivity of coupling parameter H^{m}

Fig. A.2. Comparison of two brittle fracture models for the SENT test.

conventional and exponential expressions, an internal nonlinear solver is required for damage evolution via Eq. (A.6). The general case of the CTM without constraints was derived for micromorphic models. It includes the three models mentioned above,

$$\left(\begin{bmatrix} \exp[-\mathrm{D}]\mathbb{C}^{\mathrm{e}} - \dfrac{\exp[-2\mathrm{D}]\mathbf{S}^{*}\otimes\mathbf{S}^{*}}{\exp[-\mathrm{D}]\left(\Psi^{\mathrm{e}*}-\Psi^{\mathrm{d}}_{0}-H^{\mathrm{d}}\eta+H^{\mathrm{d}}\right)+\mathbb{P}} & -\dfrac{\mathbb{P}\exp[-\mathrm{D}]\mathbf{S}^{*}}{\exp[-\mathrm{D}]\left(\Psi^{\mathrm{e}*}-\Psi^{\mathrm{d}}_{0}-H^{\mathrm{d}}\eta+H^{\mathrm{d}}\right)+\mathbb{P}} & 0 \\ -\dfrac{\mathbb{P}\exp[-\mathrm{D}]\mathbf{S}^{*}}{\exp[-\mathrm{D}]\left(\Psi^{\mathrm{e}*}-\Psi^{\mathrm{d}}_{0}-H^{\mathrm{d}}\eta+H^{\mathrm{d}}\right)+\mathbb{P}} & \dfrac{\mathbb{P}\left(\exp[-\mathrm{D}]\left(\Psi^{\mathrm{e}*}-\Psi^{\mathrm{d}}_{0}-H^{\mathrm{d}}\eta+H^{\mathrm{d}}\right)\right)}{\exp[-\mathrm{D}]\left(\Psi^{\mathrm{e}*}-\Psi^{\mathrm{d}}_{0}-H^{\mathrm{d}}\eta+H^{\mathrm{d}}\right)+\mathbb{P}} & 0 \\ 0 & 0 & A^{\mathrm{m}} \end{bmatrix}\right)_{(\mathrm{n}+1)(\mathrm{t})}, \tag{A.15}$$

$$\begin{aligned} &\mathbb{P} := \underset{\text{conventional}}{H^{\mathrm{m}}}; \\ &\mathbb{P} := \underset{\text{linear case}}{\exp\left[\widetilde{\eta}-\eta\right]\left(1-\eta+\widetilde{\eta}\right)H^{\mathrm{m}}}; \\ &\mathbb{P} := \underset{\text{exponential case}}{\exp\left[\widetilde{\eta}-\eta\right]\left(\left(q^{\mathrm{d}}+1\right)\exp\left[q^{\mathrm{d}}\left(\widetilde{\eta}-\eta\right)\right]-1\right)H^{\mathrm{m}}} \quad \text{.st. } (q^{\mathrm{d}}>0). \end{aligned} \tag{A.16}$$

For the selection of material parameters in Table A.2, the reduced (constrained) version of micromorphic quasi-brittle material is obtained:

$$\left(\begin{bmatrix} \exp[-\mathrm{D}]\mathbb{C}^{\mathrm{e}} & -\exp[-\mathrm{D}]\mathbf{S}^{*} & 0 \\ -\exp[-\mathrm{D}]\mathbf{S}^{*} & \exp[-\mathrm{D}]\left(\Psi^{\mathrm{e}*}-\Psi^{\mathrm{d}}_{0}-H^{\mathrm{d}}\eta+H^{\mathrm{d}}\right) & 0 \\ 0 & 0 & A^{\mathrm{m}} \end{bmatrix}\right)_{(\mathrm{n}+1)(\mathrm{t})}. \tag{A.17}$$

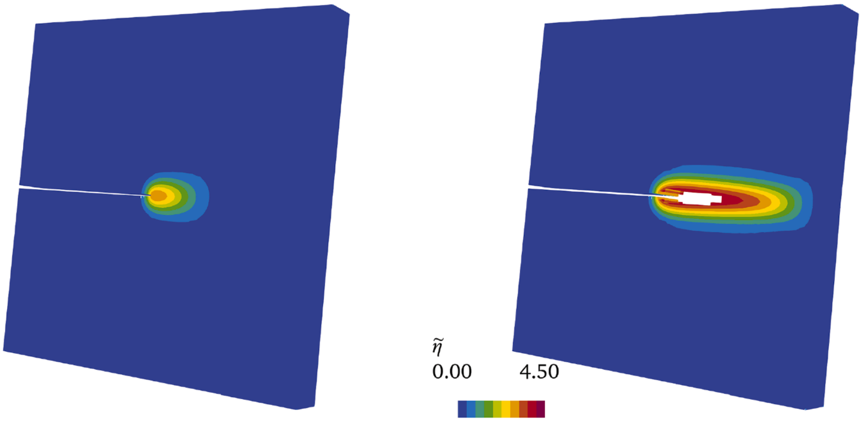

(a) Displacement = 0.0044 mm (b) Displacement = 0.005185 mm

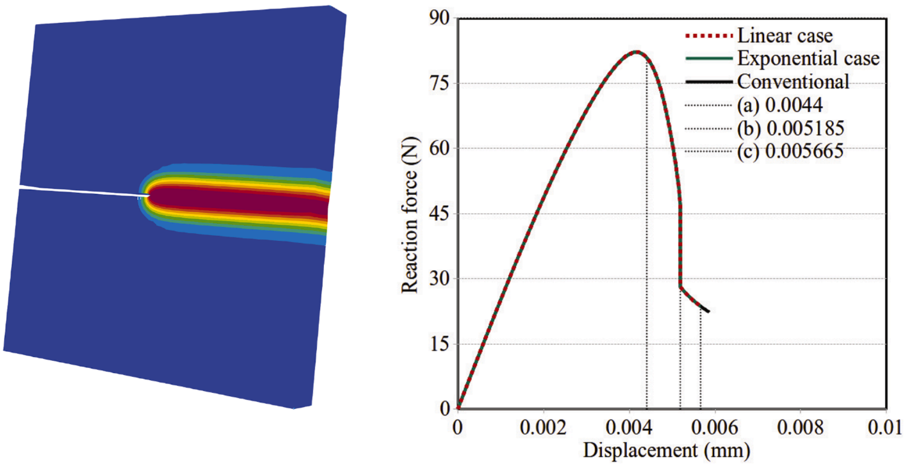

(c) Displacement = 0.005665 mm (d) Reaction–force displacement curve

Fig. A.3. Comparison of quasi-brittle fracture models for the SENT test.

The results simulated by the three distinct models should be consistent. In this case, these micromorphic models are reduced to the same damageable material model. The fully implicit damage propagation and quantitative results from the three models are summarized in Fig. A.3.

Appendix B. Verification of the sequential plasticity–damage algorithm

The sequential algorithm is straightforward to implement when damage is the sole form of inelasticity. However, when plasticity is involved, the damage process becomes highly coupled with plastic deformation, even if there is no direct plastic contribution ($\alpha = 0$) to the damage criterion. In such cases, the conventional stress-update algorithm, shown in Fig. B.1, maintains the standard finite element procedure without global robustness improvements. It is important to note that the potential active set search based on plastic and damage criteria (Fig. B.1) is completely different from the trial checking discussed in Fig. 2. Furthermore, the active set $\mathcal{A}^{\mathrm{c}}_{\mathrm{act}}$ contains information about both the plastic and damaged states. The interior linearized equation, solved via the Newton method, is used to simultaneously find the incremental time-discretized damage Lagrangian multiplier $\Delta(\Delta\gamma_{\mathrm{d}})_{(\mathrm{n}+1)(\mathrm{t})}$ and plastic multiplier $\Delta(\Delta\gamma_{\mathrm{p}})_{(\mathrm{n}+1)(\mathrm{t})}$ as [33], or multiple plastic multipliers $\Delta(\Delta\gamma^{(i)}_{\mathrm{p}})_{(\mathrm{n}+1)(\mathrm{t})}$ as in this study. This can be extremely complicated and difficult to solve locally (see Eq. (39)). Finally, the CTMs from Eq. (41) are updated for the global nonlinear iteration.

The mathematical equivalence between the two algorithms was investigated based on the isotropic constitutive material response, using the same definitions as those reported in Tan and Watanabe [33]. As shown in Fig. B.2, the comparison includes two fracture cases ($\Psi_0^{\mathrm{d}} = 0.1$ and $\Psi_0^{\mathrm{d}} = 10.0$) with the same condition ($H^{\mathrm{d}} = 5$). The algorithm parameter α, defined in Eq. (28), can be varied in the conventional algorithm. For example, a comparison was made using $\alpha = 0.9$, whereas the sequential algorithm requires the condition $\alpha = 1$ to hold. The constitutive responses of the two algorithms are in exact agreement. Additionally, the sequential algorithm demonstrated lower computational costs due to its simpler interior calculations and reduced memory usage for the "runtime" system.

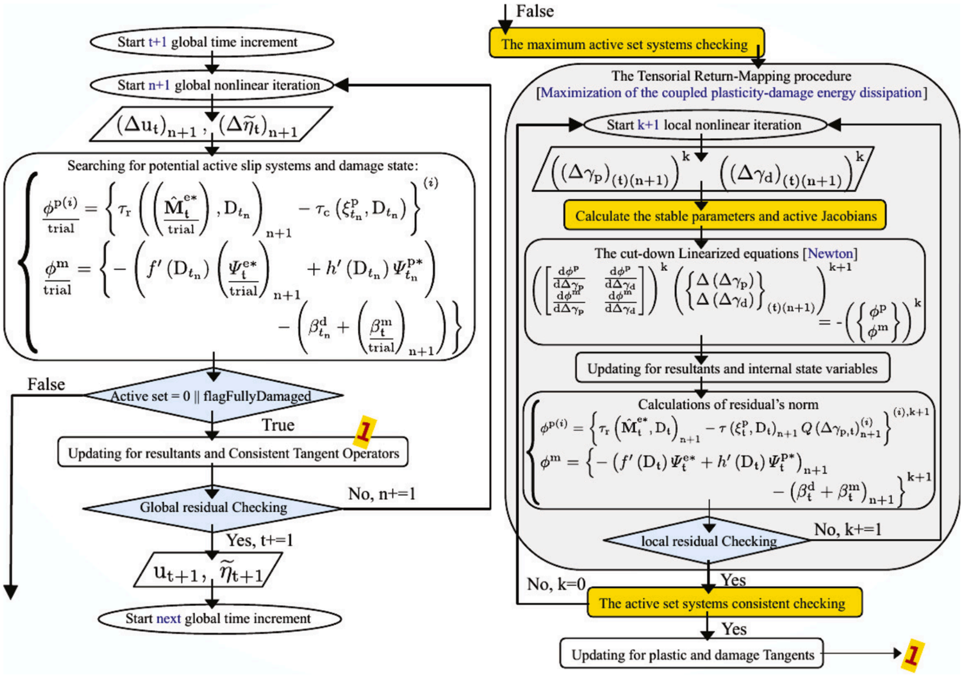

Fig. B.1. Conventional algorithm under the standard finite element procedure.

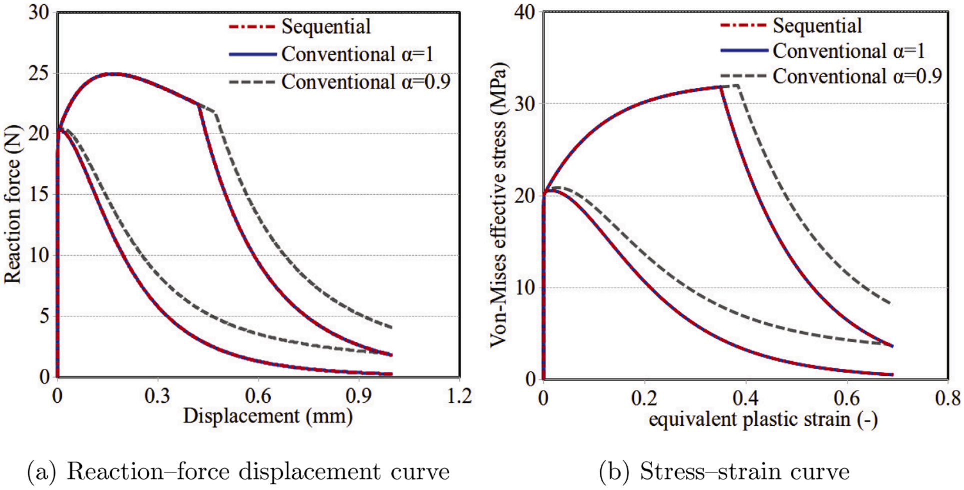

(a) Reaction–force displacement curve (b) Stress–strain curve

Fig. B.2. Algorithmic comparison by the isotropic constitutive material behavior.

References

[1] Z.P. Bazant, G. Pijaudier-Cabot, Nonlocal continuum damage, localization instability and convergence, J. Appl. Mech. 55 (2) (1988) 287–293.
[2] G.Z. Voyiadjis, P.I. Kattan, How a singularity forms in continuum damage mechanics, Mech. Res. Commun. 55 (2014) 86–88.
[3] J.C. Simo, J. Oliver, F. Armero, An analysis of strong discontinuities induced by strain-softening in rate-independent inelastic solids, Comput. Mech. 12 (5) (1993) 277–296.
[4] J. Dolbow, N. Moës, T. Belytschko, An extended finite element method for modeling crack growth with frictional contact, Comput. Methods Appl. Mech. Eng. 190 (51-52) (2001) 6825–6846.

[5] N. Moës, T. Belytschko, Extended finite element method for cohesive crack growth, Eng. Fract. Mech. 69 (7) (2002) 813–833.

[6] C. Linder, X. Zhang, A marching cubes based failure surface propagation concept for three-dimensional finite elements with non-planar embedded strong discontinuities of higher-order kinematics, Int. J. Numer. Methods Eng. 96 (6) (2013) 339–372.

[7] T. Jin, H.M. Mourad, C.A. Bronkhorst, V. Livescu, X. Zhang, C. Linder, R.A. Regueiro, Three-dimensional explicit finite element formulation for shear localization with global tracking of embedded weak discontinuities, Comput. Methods Appl. Mech. Eng. 353 (2019) 416–447.

[8] T. Heister, M.F. Wheeler, T. Wick, A primal-dual active set method and predictor-corrector mesh adaptivity for computing fracture propagation using a phase-field approach, Comput. Methods Appl. Mech. Eng. 290 (2015) 466–495.

[9] A. Mesgarnejad, B. Bourdin, M. Khonsari, Validation simulations for the variational approach to fracture, Comput. Methods Appl. Mech. Eng. 290 (2015) 420–437.

[10] R. Bharali, S. Goswami, C. Anitescu, T. Rabczuk, A robust monolithic solver for phase-field fracture integrated with fracture energy based arc-length method and under-relaxation, Comput. Methods Appl. Mech. Eng. 394 (2022) 114927.

[11] T. Jin, Z. Li, K. Chen, A novel phase-field monolithic scheme for brittle crack propagation based on the limited-memory BFGS method with adaptive mesh refinement, Int. J. Numer. Methods Eng. 125 (22) (2024) e7572.

[12] A. Kopaničáková, H. Kothari, R. Krause, Nonlinear field-split preconditioners for solving monolithic phase-field models of brittle fracture, Comput. Methods Appl. Mech. Eng. 403 (2023) 115733.

[13] J. Nocedal, S. Wright, Numerical Optimization, Springer Science & Business Media, 2006.

[14] G.A. Francfort, J.-J. Marigo, Revisiting brittle fracture as an energy minimization problem, J. Mech. Phys. Solids 46 (8) (1998) 1319–1342.

[15] J.-Y. Wu, Robust numerical implementation of non-standard phase-field damage models for failure in solids, Comput. Methods Appl. Mech. Eng. 340 (2018) 767–797.

[16] P.K. Kristensen, E. Martínez-Pañeda, Phase field fracture modelling using quasi-Newton methods and a new adaptive step scheme, Theor. Appl. Fract. Mech. 107 (2020) 102446.

[17] E. Storvik, J.W. Both, J.M. Sargado, J.M. Nordbotten, F.A. Radu, An accelerated staggered scheme for variational phase-field models of brittle fracture, Comput. Methods Appl. Mech. Eng. 381 (2021) 113822.

[18] K. Seleš, Z. Tomić, Z. Tonković, Microcrack propagation under monotonic and cyclic loading conditions using generalised phase-field formulation, Eng. Fract. Mech. 255 (2021) 107973.

[19] H.K. Akpama, M.B. Bettaieb, F. Abed-Meraim, Numerical integration of rate-independent BCC single crystal plasticity models: comparative study of two classes of numerical algorithms, Int. J. Numer. Methods Eng. 108 (5) (2016) 363–422.

[20] S. Prüger, B. Kiefer, A comparative study of integration algorithms for finite single crystal (visco-) plasticity, Int. J. Mech. Sci. 180 (2020) 105740.

[21] K. Terada, I. Watanabe, Computational aspects of tangent moduli tensors in rate-independent crystal elastoplasticity, Comput. Mech. 40 (2007) 497–511.

[22] M. Ekh, R. Lillbacka, K. Runesson, A model framework for anisotropic damage coupled to crystal (visco) plasticity, Int. J. Plast. 20 (12) (2004) 2143–2159.

[23] J. Park, K. Lee, J.-H. Kang, J.-Y. Kang, S.H. Hong, S.W. Kwon, M.-G. Lee, Hierarchical microstructure based crystal plasticity-continuum damage mechanics approach: model development and validation of rolling contact fatigue behavior, Int. J. Plast. 143 (2021) 103025.

[24] N. Zhao, A. Roy, W. Wang, L. Zhao, V.V. Silberschmidt, Coupling crystal plasticity and continuum damage mechanics for creep assessment in Cr-based power-plant steel, Mech. Mater. 130 (2019) 29–38.

[25] X. Tu, A. Ray, S. Ghosh, A coupled crystal plasticity FEM and phase-field model for crack evolution in microstructures of 7000 series aluminum alloys, Eng. Fract. Mech. 230 (2020) 106970.

[26] R. De Borst, L.J. Sluys, H.-B. Muhlhaus, J. Pamin, Fundamental issues in finite element analyses of localization of deformation, Eng. Comput. 10 (2) (1993) 99–121.

[27] R. De Borst, M.A. Crisfield, J.J.C. Remmers, C.V. Verhoosel, Nonlinear Finite Element Analysis of Solids and Structures, John Wiley & Sons, 2012.

[28] M. Neuner, R.A. Regueiro, C. Linder, A unified finite strain gradient-enhanced micropolar continuum approach for modeling quasi-brittle failure of cohesive-frictional materials, Int. J. Solids Struct. 254 (2022) 111841.

[29] S. Forest, Micromorphic approach for gradient elasticity, viscoplasticity, and damage, J. Eng. Mech. 135 (3) (2009) 117–131.

[30] S. Forest, Nonlinear regularization operators as derived from the micromorphic approach to gradient elasticity, viscoplasticity and damage, Proc. R. Soc. A Math. Phys. Eng. Sci. 472 (2188) (2016) 20150755.

[31] B. Kiefer, T. Waffenschmidt, L. Sprave, A. Menzel, A gradient-enhanced damage model coupled to plasticity-multi-surface formulation and algorithmic concepts, Int. J. Damage Mech. 27 (2) (2018) 253–295.

[32] T. Brepols, S. Wulfinghoff, S. Reese, A gradient-extended two-surface damage-plasticity model for large deformations, Int. J. Plast. 129 (2020) 102635.

[33] T. Tan, I. Watanabe, Gradient-enhanced ductile fracture constitutive modeling in implicit two-scale finite element analysis, J. Mech. Phys. Solids 196 (2025) 106025.

[34] A. Harandi, M. Tabib, B. Alatassi, T. Brepols, S. Rezaei, S. Reese, A comparative study between phase-field and micromorphic gradient-extended damage models for brittle fracture, PAMM 22 (1) (2023) e202200192.

[35] P.A. Sabnis, S. Forest, J. Cormier, Microdamage modelling of crack initiation and propagation in FCC single crystals under complex loading conditions, Comput. Methods Appl. Mech. Eng. 312 (2016) 468–491.

[36] C. Ling, S. Forest, J. Besson, B. Tanguy, F. Latourte, A reduced micromorphic single crystal plasticity model at finite deformations. Application to strain localization and void growth in ductile metals, Int. J. Solids Struct. 134 (2018) 43–69.

[37] J.-M. Scherer, J. Besson, S. Forest, J. Hure, B. Tanguy, A strain gradient plasticity model of porous single crystal ductile fracture, J. Mech. Phys. Solids 156 (2021) 104606.

[38] V. Tvergaard, A. Needleman, Analysis of the cup-cone fracture in a round tensile bar, Acta Metall. 32 (1) (1984) 157–169.

[39] A.L. Gurson, Continuum theory of ductile rupture by void nucleation and growth: Part I-yield criteria and flow rules for porous ductile media, J. Eng. Mater. Technol. 99 (1) (1977) 2–15.

[40] X. Han, J. Besson, S. Forest, B. Tanguy, S. Bugat, A yield function for single crystals containing voids, Int. J. Solids Struct. 50 (14-15) (2013) 2115–2131.

[41] L. Yu, H. Sui, W. Liu, L. Chen, Y. Liu, H. Duan, A yield criterion for porous crystalline materials with inner pressure, Int. J. Solids Struct. 202 (2020) 511–520.

[42] C. Miehe, Multisurface thermoplasticity for single crystals at large strains in terms of Eulerian vector updates, Int. J. Solids Struct. 33 (20-22) (1996) 3103–3130.

[43] J.-L. Chaboche, Description Thermodynamique et Phénoménologique de la Viscoélasticité Cyclique avec Endommagement, Ph.D. Thesis, University Pierre and Marie Curie, Paris VI, 1978.

[44] J. Lemaitre, A three-dimensional ductile damage model applied to deep-drawing forming limits, in: Mechanical Behaviour of Materials, Elsevier, 1984, pp. 1047–1053.

[45] J. Lemaitre, R. Desmorat, M. Sauzay, Anisotropic damage law of evolution, Eur. J. Mech. A. Solids 19 (2) (2000) 187–208.

[46] J. Lemaitre, A Course on Damage Mechanics, Springer Science & Business Media, 2012.

[47] P.I. Kattan, G.Z. Voyiadjis, Damage Mechanics with Finite Elements: Practical Applications with Computer Tools, Springer Science & Business Media, 2012.

[48] E.H. Lee, Elastic-plastic deformation at finite strains, J. Appl. Mech. 36 (1) (1969) 1.

[49] R.J. Asaro, Crystal plasticity, J. Appl. Mech. 50 (4B) (1983) 921–934.

[50] I. Watanabe, K. Terada, E.A. de Souza Neto, D. Perić, Characterization of macroscopic tensile strength of polycrystalline metals with two-scale finite element analysis, J. Mech. Phys. Solids 56 (3) (2008) 1105–1125.

[51] M.E. Gurtin, A gradient theory of single-crystal viscoplasticity that accounts for geometrically necessary dislocations, J. Mech. Phys. Solids 50 (1) (2002) 5–32.

[52] M.E. Gurtin, E. Fried, L. Anand, The Mechanics and Thermodynamics of Continua, Cambridge University Press, 2010.

[53] N. Ohno, D. Okumura, Higher-order stress and grain size effects due to self-energy of geometrically necessary dislocations, J. Mech. Phys. Solids 55 (9) (2007) 1879–1898.

[54] D. Peirce, R.J. Asaro, A. Needleman, Material rate dependence and localized deformation in crystalline solids, Acta Metall. 31 (12) (1983) 1951–1976.

[55] C. Miehe, J. Schröder, A comparative study of stress update algorithms for rate-independent and rate-dependent crystal plasticity, Int. J. Numer. Methods Eng. 50 (2) (2001) 273–298.

[56] I. Watanabe, K. Terada, M. Akiyama, Two-scale analysis for deformation-induced anisotropy of polycrystalline metals, Comput. Mater. Sci 32 (2) (2005) 240–250.

[57] C. Miehe, F. Welschinger, M. Hofacker, Thermodynamically consistent phase-field models of fracture: variational principles and multi-field FE implementations, Int. J. Numer. Methods Eng. 83 (10) (2010) 1273–1311.

[58] C. Miehe, L.-M. Schaenzel, H. Ulmer, Phase field modeling of fracture in multi-physics problems. Part I. Balance of crack surface and failure criteria for brittle crack propagation in thermo-elastic solids, Comput. Methods Appl. Mech. Eng. 294 (2015) 449–485.

[59] M. Ambati, T. Gerasimov, L. De Lorenzis, A review on phase-field models of brittle fracture and a new fast hybrid formulation, Comput. Mech. 55 (2015) 383–405.

[60] K. Seleš, T. Lesičar, Z. Tonković, J. Sorić, A residual control staggered solution scheme for the phase-field modeling of brittle fracture, Eng. Fract. Mech. 205 (2019) 370–386.

[61] G. Giudicelli, A. Lindsay, L. Harbour, C. Icenhour, M. Li, J.E. Hansel, P. German, P. Behne, O. Marin, R.H. Stogner, J.M. Miller, D. Schwen, Y. Wang, L. Munday, S. Schunert, B.W. Spencer, D. Yushu, A. Recuero, Z.M. Prince, M. Nezdyur, T. Hu, Y. Miao, Y.S. Jung, C. Matthews, A. Novak, B. Langley, T. Truster, N. Nobre, B. Alger, D. Andrš, F. Kong, R. Carlsen, A.E. Slaughter, J.W. Peterson, D. Gaston, C. Permann, 3.0 - MOOSE: enabling massively parallel multiphysics simulations, SoftwareX 26 (2024) 101690. https://www.sciencedirect.com/science/article/pii/S235271102400061X. https://doi.org/10.1016/j.softx.2024.101690

[62] L. Anand, M. Kothari, A computational procedure for rate-independent crystal plasticity, J. Mech. Phys. Solids 44 (4) (1996) 525–558.

[63] S. Ganesan, Microstructural Response of Magnesium Alloys: 3D Crystal Plasticity and Experimental Validation, Ph.D. Thesis, University of California, Santa Barbara, 2017.

[64] J. Zhang, T. Brepols, S. Reese, A two-surface damage-plasticity model based on a Drucker-Prager yield criterion, PAMM 22 (1) (2023) e202200296.

[65] I. Watanabe, D. Setoyama, N. Iwata, K. Nakanishi, Characterization of yielding behavior of polycrystalline metals with single crystal plasticity based on representative characteristic length, Int. J. Plast. 26 (4) (2010) 570–585.

[66] E.A. de Souza Neto, D. Perić, M. Dutko, D. Owen, Design of simple low order finite elements for large strain analysis of nearly incompressible solids, Int. J. Solids Struct. 33 (20-22) (1996) 3277–3296.

[67] E.A. de Souza Neto, D. Peric, D.R.J. Owen, Computational Methods for Plasticity: Theory and Applications, John Wiley & Sons, 2011.

[68] S. Felder, N. Kopic-Osmanovic, H. Holthusen, T. Brepols, S. Reese, Thermo-mechanically coupled gradient-extended damage-plasticity modeling of metallic materials at finite strains, Int. J. Plast. 148 (2022) 103142.

[69] J.-Y. Wu, A unified phase-field theory for the mechanics of damage and quasi-brittle failure, J. Mech. Phys. Solids 103 (2017) 72–99.